The metabolic signaling of the nucleoredoxin-like 2 gene supports brain function

Céline Jaillard, Farah Ouechtati, Emmanuelle Clérin, Géraldine Millet-Puel, Mariangela Corsi, Najate Aït-Ali, Frédéric Blond, Quentin Chevy, Lara Gales, Mélissa Farinelli, et al.

Redox Biology 48 (2021) 102198

Contents lists available at ScienceDirect

Redox Biology

journal homepage: www.elsevier.com/locate/redox

The metabolic signaling of the nucleoredoxin-like 2 gene supports brain function

Céline Jaillard [a,1], Farah Ouechtati [a,1], Emmanuelle Clérin [a,1], Géraldine Millet-Puel [a,1], Mariangela Corsi [a], Najate Aït-Ali [a], Frédéric Blond [a], Quentin Chevy [b], Lara Gales [c], Mélissa Farinelli [d], Deniz Dalkara [a], José-Alain Sahel [a], Jean-Charles Portais [c], Jean-Christophe Poncer [b], Thierry Léveillard [a,*]

[a] Sorbonne Université, INSERM, CNRS, Institut de la Vision, F-7501b, Paris, France
[b] Sorbonne Université, INSERM, CNRS, Institut du Fer à Moulin, F-75005, Paris, France
[c] MetaToul-MetaboHUB, National Infrastructure of Metabolomics & Fluxomics, 31077, Toulouse, France
[d] E-Phy-Science, Bioparc de Sophia Antipolis, 2400 route des Colles, 06410, Biot, France

ARTICLE INFO

Keywords:
Glucose metabolism
Thioredoxin
Tauopathy
Long-term potentiation
Metabolomics
Hippocampus
Area postrema
Gene therapy

ABSTRACT

The nucleoredoxin gene *NXNL2* encodes for two products through alternative splicing, rod-derived cone viability factor-2 (RdCVF2) that mediates neuronal survival and the thioredoxin-related protein (RdCVF2L), an enzyme that regulates the phosphorylation of TAU. To investigate the link between *NXNL2* and tauopathies, we studied the *Nxnl2* knockout mouse (*Nxnl2*$^{-/-}$). We established the expression pattern of the *Nxnl2* gene in the brain using a *Nxnl2* reporter mouse line, and characterized the behavior of the *Nxnl2*$^{-/-}$ mouse at 2 months of age. Additionally, long term potentiation and metabolomic from hippocampal specimens were collected at 2 months of age. We studied TAU oligomerization, phosphorylation and aggregation in *Nxnl2*$^{-/-}$ brain at 18 months of age. Finally, newborn *Nxnl2*$^{-/-}$ mice were treated with adeno-associated viral vectors encoding for RdCVF2, RdCVF2L or both and measured the effect of this therapy on long-term potential, glucose metabolism and late-onset tauopathy. *Nxnl2*$^{-/-}$ mice at 2 months of age showed severe behavioral deficiency in fear, pain sensitivity, coordination, learning and memory. The *Nxnl2*$^{-/-}$ also showed deficits in long-term potentiation, demonstrating that the *Nxnl2* gene is involved in regulating brain functions. Dual delivery of RdCVF2 and RdCVF2L in newborn *Nxnl2*$^{-/-}$ mice fully correct long-term potentiation through their synergistic action. The expression pattern of the *Nxnl2* gene in the brain shows a predominant expression in circumventricular organs, such as the *area postrema*. Glucose metabolism of the hippocampus of *Nxnl2*$^{-/-}$ mice at 2 months of age was reduced, and was not corrected by gene therapy. At 18-month-old *Nxnl2*$^{-/-}$ mice showed brain stigmas of tauopathy, such as oligomerization, phosphorylation and aggregation of TAU. This late-onset tauopathy can be prevented, albeit with modest efficacy, by recombinant AAVs administrated to newborn mice. The *Nxnl2*$^{-/-}$ mice have memory dysfunction at 2-months that resembles mild-cognitive impairment and at 18-months exhibit tauopathy, resembling to the progression of Alzheimer's disease. We propose the *Nxnl2*$^{-/-}$ mouse is a model to study multistage aged related neurodegenerative diseases. The *NXNL2* metabolic and redox signaling is a new area of therapeutic research in neurodegenerative diseases.

1. Introduction

The nucleoredoxin-like 2 (*NXNL2*) gene, the paralogue of *NXNL1*, expresses two protein products by alternative splicing [1], the short rod-derived cone viability factor 2 (RdCVF2) and the longer thioredoxin-related protein RdCVF2L. We have previously reported that the inactivation of the *Nxnl2* gene in the mouse results in a progressive deficit of vision and olfaction [2]. The extracellular protein RdCVF2 improves cone survival *in vitro* and the RdCVF2L protein prevents *in vivo* the phosphorylation of the microtubule associated protein τ (TAU),

* Corresponding author. Department of Genetics, Institut de la Vision, 17, rue Moreau, 75012, Paris, France.
E-mail address: thierry.leveillard@inserm.fr (T. Léveillard).
[1] Equal contribution.

https://doi.org/10.1016/j.redox.2021.102198
Received 10 November 2021; Accepted 22 November 2021
Available online 25 November 2021

induced in the retina in response to light damage [3]. TAU is an intrinsically disordered protein which facilitates the assembly and stability of neuronal microtubules. Under pathological conditions, collectively known as tauopathies, TAU becomes hyperphosphorylated and detaches from microtubules, leading to the misfolding and formation of TAU aggregates forming neurofibrillary tangles (NFT). These are the hallmarks of several neurodegenerative diseases, such as Alzheimer's disease and frontotemporal dementia with parkinsonism linked to chromosome 17 (FTDP-17).

In the retina, considered an extension of the brain, the role of *NXNL2* is partially redundant to that of *NXNL1*. *NXNL1* which encodes two products through alternative splicing: RdCVF a protein secreted by rods photoreceptors and RdCVFL protecting rods and cones against damaging oxidation [4,5]. The delivery of both products of the *NXNL1* gene, RdCVF and RdCVFL, is a promising future therapy for treating a broad range of retinal diseases, independent of genetic mutations [6]. The protective effect of RdCVF on cones results from its ability to stimulate cones' glucose uptake via its interaction at the cell-surface of the cell with a complex formed between basigin-1 (BSG1) and the glucose transporter GLUT1 (SLC2A1) [7]. Glucose taken up by cones is metabolized through aerobic glycolysis, a partial anabolic metabolic pathway required for the renewal of the outer segments of photoreceptors, the neuronal structure where reside the light sensing opsins [8,9]. RdCVFL interacts physically with TAU in the retina and prevents its phosphorylation and aggregation [4,10]. The presumed thiol-oxidoreductase activity of RdCVFL relies on the production of NADPH by the metabolism of glucose through the pentose phosphate pathway (PPP) [11], so the action of RdCVF via BSG1/GLUT1 potentiates the redox power of the thioredoxin-related protein RdCVFL [12]. The two intricate activities of the *NXNL1* gene products in the retina are essential to protect photoreceptors against starvation and oxidative damages constituting an endogenous neuroprotective metabolic and redox signaling [13].

Here, we observed that cognitive deficits precede sensory deficits of the *Nxnl2*$^{-/-}$ mouse. A systematic analysis of the behavior of young animals reveals a deficit in memory that was shown to result from a dysfunction of the hippocampus. This cognitive deficit evolves in aged animals into a tauopathy, a sequence of events resembling the clinical scenario in patients developing Alzheimer's disease [14].

2. Results

2.1. The behavior of the mouse with a targeted inactivation of the nucleoredoxin-like 2 geneis syndromic

We initially observed that *Nxnl2*$^{-/-}$ mice were hyperactive as compared to *Nxnl2*$^{+/+}$ wild type controls, but also to *Nxnl1*−/− mice created on the same genetic background using the same technology. We performed a global behavioral analysis, reported here ordered by test sessions, using two groups of 12 ♂ mice at 2 months of age (Fig. 1). The use of only one sex was justified by the objective of getting more homogenous results and does not reflect any presumed biological gender distinction [15]. The animals were monitored for spontaneous water and food intake and rear activity during three sequential phases, habituation, dark and light. *Nxnl2*$^{+/+}$ mice display an expected nocturnal drinking activity that is perturbed for *Nxnl2*$^{-/-}$ mice (Fig. 1A). During lighting periods, *Nxnl2*$^{-/-}$ are drinking more often than *Nxnl2*$^{+/+}$ mice, but this is the contrary in the dark period (Supl. Fig. 1A). A similar situation was observed for their feeding behavior, but *Nxnl2*$^{-/-}$ mice do not exhibit reduced feeding at night. In fact, over a 32-h testing period, *Nxnl2*$^{-/-}$ mice have a higher food consumption (Supl. Fig. 1B). The number of rears that scores the exploratory behavior is also perturbed for *Nxnl2*$^{-/-}$ mice which display increased vertical activity during the 32-h testing period (Supl. Fig. 1C). The disorganization of the circadian activity of mice lacking the *Nxnl2* gene is likely resulting from the loss of expression of the gene in the pineal gland, an indirectly light-sensitive part of the circadian system that harbors photoreceptor-related pinealocytes [16]. Daily profiling of *Nxnl2* gene expression in the pineal gland shows a higher level of expression during daylight. The pineal gland is a crucial structure of the circadian system that is connected to the suprachiasmatic nuclei, the central circadian clock in mammals [17]. Overall, hyperphagia occurs in the absence of weight gain for *Nxnl2*$^{-/-}$ mice (Supl. Fig. 1D), suggesting that it is a consequence of their higher rearing activity and increased general activity [18].

This is visible in the open-field test performed with 150 lx in the center of the arena. The distance traveled is longer for *Nxnl2*$^{-/-}$ mice in 5 min test sessions carried in a novel open field (Fig. 1B), and is overall longer ($p = 0.0078$). A representative path trace of the trajectories shows that the *Nxnl2*$^{+/+}$ mouse explores more often the periphery of the arena, while the *Nxnl2*$^{-/-}$ mouse crosses many times the center surface (Fig. 1C). While the traveled distance may translate to a higher general activity of *Nxnl2*$^{-/-}$ mice in agreement with the hyperactivity observed initially, the lack of aversion for brightly lit, open and unknown environments of the *Nxnl2*$^{-/-}$ mice shows that these animals have lost, at least partially, a phylogenetic anxiety-inhibitory behavior (Fig. 1D) [19].

The animals compared have similar body weight (Supl. Fig. 1D) and locomotor activity (Supl. Fig. 1E), but *Nxnl2*$^{-/-}$ mice have an average body temperature of 37.75 °C, higher to that of 37.31 °C of *Nxnl2*$^{+/+}$ mice (Supl. Fig. 1F). The core body temperature is affected by time of the day as manifested through the circadian temperature rhythm [20]. In the mouse, body temperature is controlled by circadian lipid metabolism by thermogenic brown adipose tissue whose mitochondrial uncoupling increases energy expenditure under cold-stressed conditions [21]. During daytime, the mouse prefers an ambient temperature that is just 4–6 °C below its core temperature, and consequently behavior tests, performed here at 21–22 °C are done under slightly cold-stressed conditions [22]. The temperature of *Nxnl2*$^{-/-}$ mice was measured during the day, when they are abnormally active (Supl. Fig. 1C), which can explain the difference in core body temperature with *Nxnl2*$^{+/+}$ mice. The high temperature is a possible consequence of its measurement during higher activity periods since brown adipose tissue metabolism is increased by both cold exposure and exercise [23,24], or by psychological stress-induced hyperthermia [25].

Compared mice have similar muscular strength (Supl. Fig. 1G), but *Nxnl2*$^{-/-}$ mice have a shorter mean latency in the string test (Fig. 1E). This traction reflex relies on the coordination between forelimb-hanging to gain hindlimb traction. The reduced latency shows that *Nxnl2*$^{-/-}$ mice have an over operating anteroposterior motor coordination by the cerebellum [26]. This is supported by the higher performance of *Nxnl2*$^{-/-}$ mice in a test that measures the ability of an animal to maintain balance on a rotating rod (Fig. 1F). This task requires motor coordination controlled by the cerebellum with many other regions involved in proprioceptive and vestibular functions. The mean latency before falling in the rotarod test is not correlated ($r = 0.1157$, $n = 24$) to the total distance traveled in the open field, indicating motor skills of the *Nxnl2*$^{-/-}$ mice were not acquired by increased locomotion.

The spatial and memory performance of *Nxnl2*$^{-/-}$ mice were first tested using Y-maze under 100 lx of light. The number of arm entries of *Nxnl2*$^{-/-}$ mice is higher than that of *Nxnl2*$^{+/+}$ mice (Fig. 1G), which correlates with a higher locomotor activity. The inactivation of the paralogue gene *Nxnl1*, whose expression is restricted to the retina, does not trigger this phenotype (Fig. 1H). The specific task that relies on spatial working memory is the natural tendency to choose an alternative arm over an arm previously explored what is scored as % of spontaneous alternation [27]. We observed a non-statistical trend that was confirmed to be statistically significant by adding a second cohort (Fig. 1I). The *Nxnl2*$^{-/-}$ mice do not remember correctly which arm they have previously visited, which implies a deficit in learning and memory.

We alternated working memory tests with a test of anxiety-related behavior for logistic reasons dictated by the workflow. The tail suspension test is widely used to evaluate the antidepressant-like effects of drugs [28]. The decrease in the duration of the immobility shows that

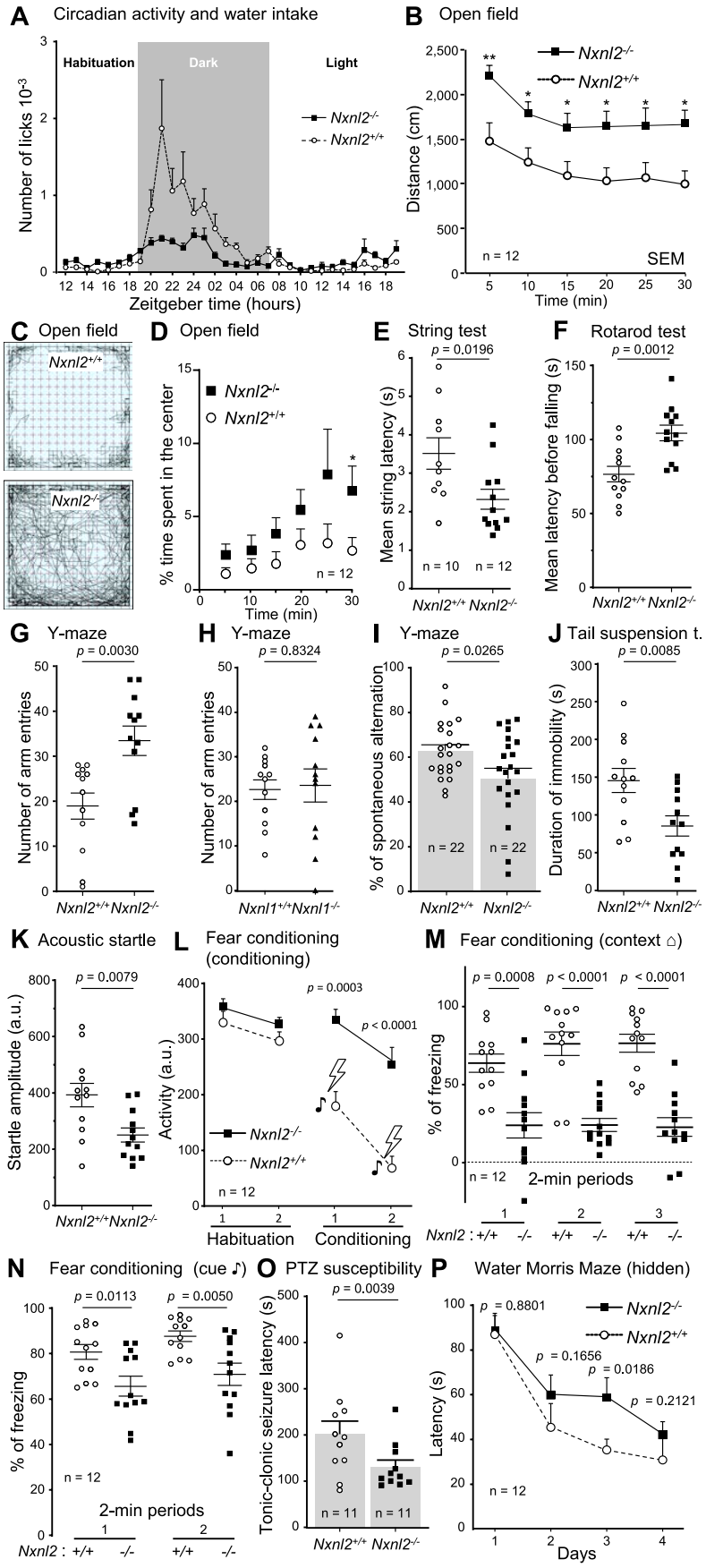

Fig. 1. The behavior of the *Nxnl2*$^{-/-}$ mouse. Two groups of 12 *Nxnl2*$^{+/+}$ and 12 *Nxnl2*$^{-/-}$ ♂ mice were tested at 2 months of age following an ordered pipeline as the results are reported here. Both groups are on a BALB/c background. (A) Circadian activity and water intake. (B–D) Open field. (E) String test. (F) Rotarod test. (G) Y-maze. (H) Y-maze using groups of 12 *Nxnl1*$^{+/+}$ and *Nxnl1*$^{-/-}$ ♂ mice (BALB/c) aged of 2 months. (I) Y-maze using and additional cohort of 10 *Nxnl2*$^{+/+}$ and 12 *Nxnl2*$^{-/-}$ ♂ mice aged of 2 months. (J) Tail suspension test. (K) Acoustic startle. (L-N) Cued and contextual fear conditioning. (O) Pentylenetetrazol (PTZ) susceptibility. (P) For water Morris maze, a novel cohort of 12 *Nxnl2*$^{+/+}$ and 12 *Nxnl2*$^{-/-}$ ♂ mice were tested at 2 months of age was used. The data are plotted with standard of the mean (SEM). The data were analyzed by t-tests using GraphPad.

Nxnl2$^{-/-}$ mice have a reduced susceptibility to despair (Fig. 1J), inversely correlated (r = −0.5893, *P* = 0.0024) to the latency of the first immobilization (Supl. Fig. 1H). This invert correlation improves the detection of antidepressant-like behavior of *Nxnl2*$^{-/-}$ mice [29] and confirms the decrease in anxiety-related behavior previously observed (Fig. 1D).

The amplitude (arbitrary units) of the acoustic startle reflex of *Nxnl2*$^{-/-}$ mice to a startling acoustic pulse of 110 dB, but not for prepulses with lower intensities (70, 80, 85 and 90 dB/10 ms) is reduced as compared to *Nxnl2*$^{+/+}$ mice (Fig. 1K). When a low-salience auditory stimulus precedes an unexpected startle-like acoustic stimulus, the startle motor reaction becomes less pronounced [30]. This phenomenon, known as prepulse inhibition, is normal for *Nxnl2*$^{-/-}$ mice (Supl. Fig. 1I). The deficit of acoustic startle reflex of *Nxnl2*$^{-/-}$ mice could translate the anxiolytic effect of the inactivation of *Nxnl2* gene [31] (Fig. 1D). Alternatively, since aged *Nxnl2*$^{-/-}$ mice have a deficit in vision and olfaction [2], we cannot rule out that the reduced amplitude of the acoustic startle reflex is translating a reduction of auditory function, even at 2 months of age.

The associative and memory performance of *Nxnl2*$^{-/-}$ mice were then tested after habituation to sessions during which a stimulus (the cue, a tone ♪) is paired with an aversive unconditioned stimulus (an electric foot-shock) [32]. *Nxnl2*$^{+/+}$ mice respond to the aversive stimulus by reducing their locomotor activity more than *Nxnl2*$^{-/-}$ mice (Fig. 1L). The following day, the percentage of freezing of *Nxnl2*$^{-/-}$ mice when replaced the same environmental context (⌂) is lower than *Nxnl2*$^{-/-}$ mice (Fig. 1M, and Supl. Fig. 1J). The percentage of freezing of *Nxnl2*$^{-/-}$ mice is also lower than *Nxnl2*$^{+/+}$ mice in response to the cue (♪) (Fig. 1N, and Supl. Fig. 1K). This points to a dysfunction of a neural circuit involving the amygdala, the cerebral cortex and the hippocampus [33]. This prompted us to look at the response to acute thermal pain of the animals that may interfere with the learning and memory test of cued and contextual fear conditioning. A heat stimulus applied to the tail does not trigger a difference in the response between the two mouse genotypes (Supl. Fig. 1L). Nevertheless, the first reaction of *Nxnl2*$^{-/-}$ mice (licking/jumping) on a 52 °C plate is delayed compared to *Nxnl2*$^{+/+}$ mice (Supl. Fig. 1M) indicating the nociceptive threshold is abnormally high for *Nxnl2*$^{-/-}$ mice. Mice exhibit a marked fear of novel stimuli [34]. Pain and anxiety are closely linked and the reduction of anxiety is accompanied by a parallel decrease in pain sensitivity [35]. The reduced latency of *Nxnl2*$^{-/-}$ mice in the hot-plate test is likely due to their anxiolytic-related behavior (Fig. 1D, J and 1K).

Intraperitoneal injection of 50 mg/kg of pentylenetetrazol (PTZ), a convulsant drug, triggers an extended latency of *Nxnl2*$^{-/-}$ mice compared to wild-type controls (Fig. 1O), but the seizure profiles are comparable. One should notice that similar antiseizure effects of PTZ-induced seizures were observed after systemic administration of fructose-1,6-bisphosphate (FBP) *in vivo* [36]. Epilepsies, characterized by convulsive frequent febrile seizures are linked to impaired brain glucose metabolism [37]. This points to a modification of the brain glucose metabolism generated by the inactivation of the *Nxnl2* gene.

Using unique cohorts allows the analysis of correlations. So, the anxiolytic-related behavior (anti-anxiety) measured during open field tests is correlated to the depression-like behavior seen by tail suspension immobility duration (Supl. Fig. 1O), which is inversely correlated to pain sensitivity measured by the hot-plate tests (Supl. Fig. 1P). Pain sensitivity is inversely correlated to sensorimotor gating, measured by acoustic startle reactivity (r = −0.4759, *p* = 0.0187) and to sensorimotor abilities, measured by string tests (r = −0.4993, *p* = 0.0180). Sensorimotor abilities (string tests) are correlated to PTZ sensibility (r = 0.4518, *p* = 0.0455, *n* = 11) and inversely correlated to core body temperature (r = −0.5132, *p* = 0.0146). Sensorimotor abilities measured by the rotarod test is correlated to pain sensitivity measured by the hot-plate test (r = 0.4176, *p* = 0.0423). Learning and memory measured by spontaneous alternation in the Y-maze is inversely correlated to sensorimotor abilities tested in the rotarod test (r = −0.4728, *p* = 0.0263). The inactivation of the *Nxnl2* gene triggers a complex syndrome in which fear, pain sensitivity, coordination, learning and memory and possibly brain glucose metabolism are deficient what could be translated by an abnormally high core body temperature. The anxiolytic effect is regulated by the amygdala that is connected to the temporal two-thirds of the distal portion of hippocampal *Cornu Ammonis* (CA)1 region [38].

To address learning and memory in a test that does not depend on pain sensitivity, we used a novel cohort of ♂ to test the animals under 100 lx of ambient light in the Morris water maze at water temperature of 20–21 °C. After training, the latency to reach the visible platform of the *Nxnl2*$^{-/-}$ mice is longer than for the *Nxnl2*$^{+/+}$ control mice (Supl. Fig. 1N). When the platform was hidden under the surface of water, a deficit in latency was also observed for *Nxnl2*$^{-/-}$ mice (Fig. 1P). Mice of both genotypes ameliorate every day their performance in the test using either visible or hidden platform, but while the deficit of *Nxnl2*$^{-/-}$ mice is observed from the first day with the visible platform, it is only perceptible at day two and statistically significant at day three with the hidden platform. The performances of this test rely on hippocampal-dependent visuospatial navigation [39]. The vision of *Nxnl2*$^{-/-}$ mice starts to deteriorate only after two months of age which cannot impairs with the test performed here on 2-month animals [2].

2.2. Impaired hippocampal plasticity upon nucleoredoxin-like 2 gene inactivation

The *Nxnl2*$^{-/-}$ syndrome encompasses many deficits in hippocampal-dependent learning and memory. Long-term potentiation (LTP) at the CA3 to CA1 hippocampal synapses are one the biological mechanisms supporting learning of goal-directed spatial task [40]. Thus, we aimed at investigating whether hippocampal LTP could be altered in *Nxnl2*$^{-/-}$ mice. We performed *ex vivo* extracellular recordings of field excitatory postsynaptic potentials (fEPSP) in the CA1 region while stimulating Schaffer collateral originating from CA3 (Additional file 1). We recorded several slices per animals. The postsynaptic recordings are distinct between the two genotypes (Supl. Fig. 2A). In 10 slices from 3 *Nxnl2*$^{+/+}$ mice, high frequency stimulation (HFS) induced a long-lasting (>50 min), >2-fold increase in fEPSP amplitude compared to baseline (+168 ± 59) (Supl. Fig. 2B). In contrast, this form of LTP was significantly reduced and almost abolished (+10.6 ± 22%) in slices from *Nxnl2*$^{-/-}$ mice (Supl. Fig. 2C) [41].

We repeated the analysis of LTP by comparing that of the *Nxnl2*$^{-/-}$ mouse (BALB/c background) to an additional mouse model constructed by inserting a β-galactosidase reporter within the *Nxnl2* locus of mice with C57Bl/6-N background (Supl. Fig. 2D). The *Nxnl2*$^{-/-}$ was constructed by deleting exon 1, encoding for RdCVF2, by homologous recombination [2] (Fig. 2A). For the homozygous reporter mice (*Nxnl2*$^{R/R}$), the introduction of the reporter cassette erases the sequence of both RdCVF2 and RdCVF2L (Fig. 2E). Recording from this new mouse model showed similar results: LTP at CA3-CA1 was altered upon inactivation of *Nxnl2* gene for *Nxnl2*$^{-/-}$ (Fig. 2B, C, D) and *Nxnl2*$^{R/R}$ (Fig. 2F, G, H). The two mouse models of *Nxnl2* inactivation were produced in distinct genetic backgrounds (BALB/c and C57B/L6N), which reinforce the argument that the deficit is linked to the inactivation of the *Nxnl2* gene. Importantly, the basal synaptic transmission did not appear altered in either of these mouse models for *Nxnl2* inactivation as shown by the similar stimulus-response curves to those obtained from control animals (Supl. Fig. 2E, F). Overall, these electrophysiological recordings show alteration in hippocampal plasticity upon *Nxnl2* deletion that could support spatial memory deficit.

2.3. The nucleoredoxin-like 2 gene is expressed in the area postrema

A corollary to the deficit in brain function of the *Nxnl2*$^{-/-}$ is that the *Nxnl2* gene must be expressed in the brain. For the reporter allele R, β-galactosidase expression is presumably under the control of the

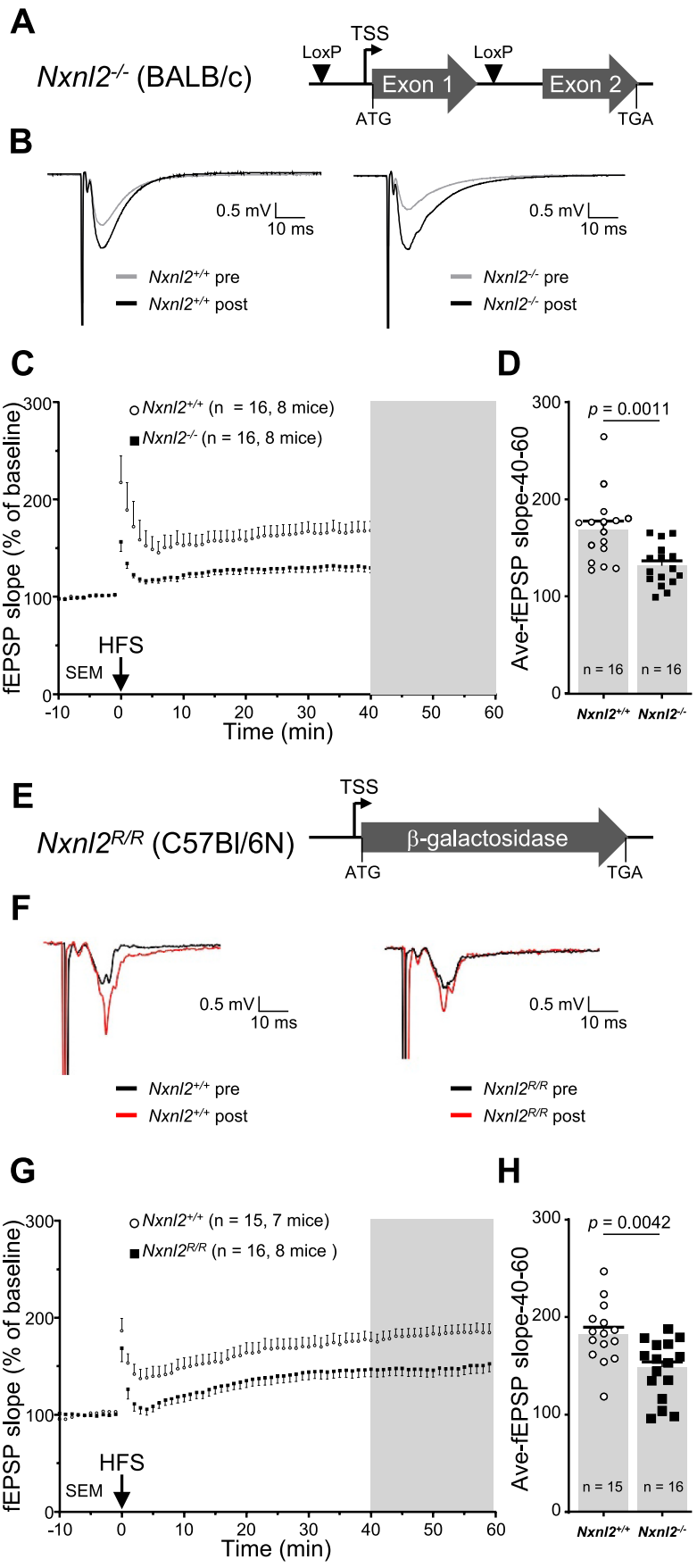

Fig. 2. The *Nxnl2*$^{-/-}$ has an impaired function of the hippocampus. (A) Schematic representation of the recombination of the *Nxnl2* gene on a BALB/c background. The recombination of the Lox-P sites removes the sequence of exon 1 that encodes for RdCVF2 (Q9D531-4). The exon 2 does not contain for any in-frame methionine, RdCVF2L (Q9D531-3) is not expressed by the *Nxnl2*$^{-/-}$ mouse. (B) Representative traces of the pre- and post-HFS on hippocampal slices from mice aged of two months. (C) Recording of field excitatory postsynaptic potentials (fEPSP) slope normalized to the baseline for 60 min following HFS. The number of animals and hippocampal slices is indicated. (D) Average fEPSP slope recorded between 40 and 60 min following HFS. (E) Schematic representation of the recombination of the *Nxnl2* gene on a C57BL/6-N background with the insertion of a β-galactosidase reporter between the ATG and the TGA of RdCVF2L (Q9D531-3). TSS: transcriptional start site. ^{R}: the β-galactosidase allele. The data are plotted with SEM. The data were analyzed by t-tests using GraphPad. (F) Representative traces of the pre- and post-HFS recordings on hippocampal slices from mice aged of two months. (G) Recording of fEPSP slope normalized to the baseline for 60 min following HFS. The number of animals and hippocampal slices is indicated. (H) Average fEPSP slope recorded between 40 and 60 min following HFS.

endogenous *Nxnl2* promoter, located in 5' on its open reading frame, as shown in the retina [42]. In this configuration, the reporter will not distinguish the expression of RdCVF2L from that of RdCVF2, the later resulting from intron retention. Nevertheless, β-galactosidase staining of mouse tissues indicates the regionalization of *Nxnl2* expression, taken as a whole. As expected from a previous study, the *Nxnl2*$^{R/+}$ mouse at 2 months showed signals in the olfactory tube [2] (Supl. Fig. 3A). At higher resolution, the staining can be delineated to the olfactory sensitive neurons (Supl. Fig. 3B). These receptor neurons project their axons to the glomerular layer of the olfactory bulb (Supl. Fig. 3C). The adequacy between the β-galactosidase staining pattern and what is known of *Nxnl2* expression confirms that the *Nxnl2*$^{R/+}$ mouse is an appropriate model to explore *Nxnl2* expression in the brain. We sectioned the brain of a *Nxnl2*$^{R/+}$ mouse at 2 months to reveal the endogenous expression of the *Nxnl2* gene at that age. We compared the blue coloration of stained sections of thirty-five regions of the *Nxnl2*$^{R/+}$ brain to that of the negative control (*Nxnl2*$^{+/+}$, C57BL/6-N), both at 2-month of age DOI 10.25493/4975-NDG. We detected scattered signals mapping to regions involved in the behavior that is altered in the *Nxnl2*$^{-/-}$ mouse, such as the hippocampic formation, the central, lateral, basolateral and basomedial nuclei of the amygdala, and throughout many other brain regions [43]. For example, *Nxnl2* expression in the subiculum which is the main hippocampal exit through afferent ways from CA1. The most prominent and ordered signal was observed in the *area postrema* (Fig. 3A). The expression of the reporter protein was restricted to a subset of cells of the *area postrema* [44] (Fig. 3B). The *area postrema* is a member of the circumventricular organs composed of fenestrated capillaries with discontinuous expression of tight junction and extensive interactions of parenchymal cells of this organ with the cerebrospinal fluid (CSF) and blood circulation [45]. The reporter signal is increased in the *area postrema* of the *Nxnl2*$^{R/R}$ mouse, which indicates that the survival of *Nxnl2* expressing cells of the *area postrema* does not require the action of the *Nxnl2* gene, at least up to 2 months (Supl. Fig. 3D). Similar observations were made for another circumventricular organ, such as the subfornical organ involved in thirst and hunger (Supl. Fig. 3E) [46]. The sensory subfornical organ in the forebrain, as the *area postrema* in the hindbrain, lacks a normal blood-brain barrier such that neurons, within them, are exposed to blood-borne agents. This is also true for an adjacent positive region, the median preoptic nucleus that is involved in core body thermoregulation (Supl. Fig. 3F) [47]. Neurons in the median

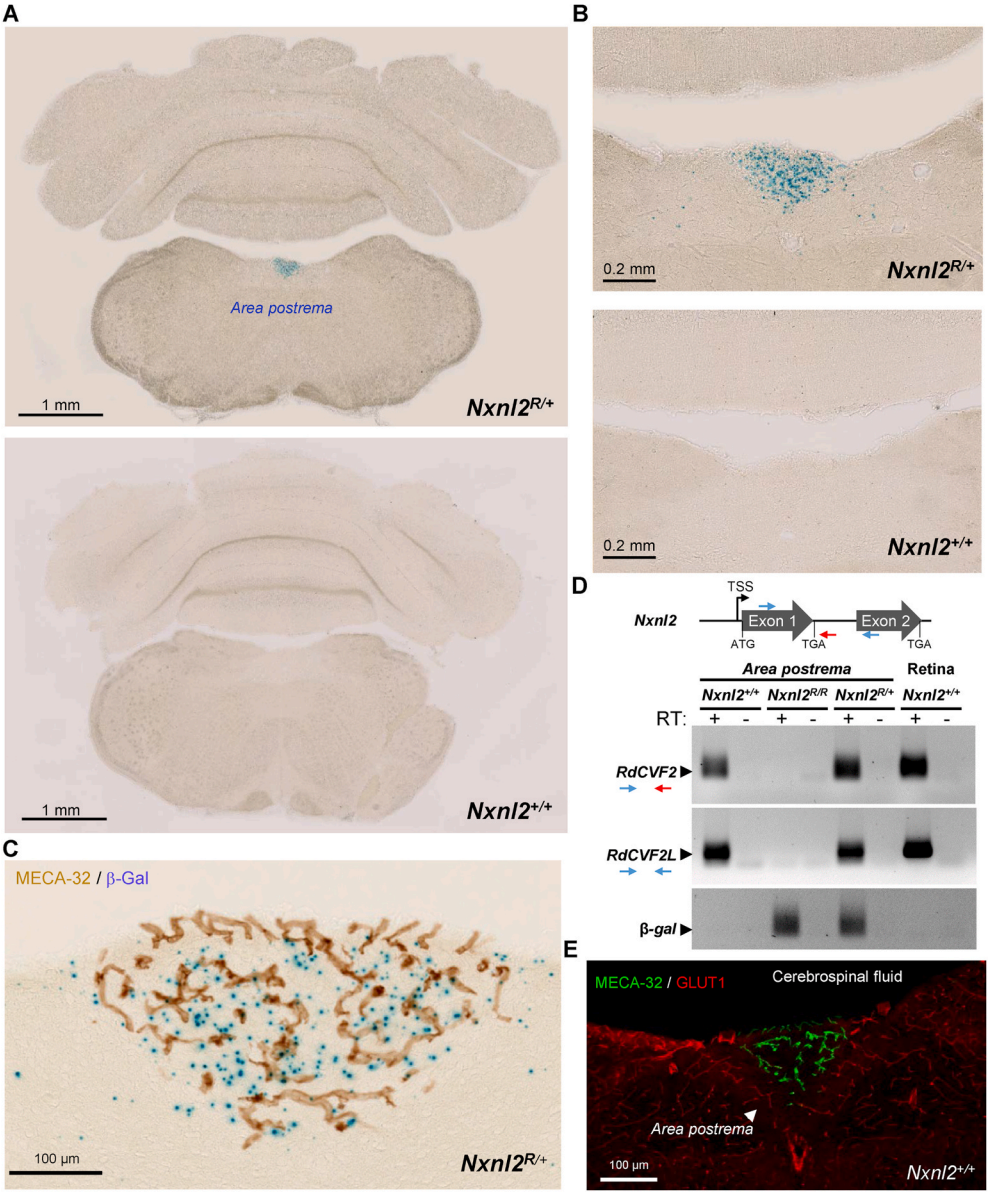

Fig. 3. *Nxnl2* is expressed in a subset of cells of the *area postrema*. (A) β-galactosidase staining of brain sections of a *Nxnl2*$^{R/+}$ and its control, a *Nxnl2*$^{+/+}$ mouse at 2 months of age. (B) Higher magnification. (C) Immunohistochemical detection of PLVAP/MECA-32 on an *area postrema* section of a *Nxnl2*$^{R/+}$ mouse at two months of age, pre-stained for β-galactosidase activity (β-Gal). (D) Expression of RdCVF2, RdCV2L and β-galactosidase (*β-gal*) mRNAs in *area postrema* specimens of the *Nxnl2*$^{+/+}$, *Nxnl2*$^{R/R}$ and *Nxnl2*$^{R/+}$ 2-month mice. The retina was used as positive control. RT: reverse transcriptase. (E) Immunofluorescent detection of both PLVAP/MECA-32 and the glucose transporter GLUT1 on an *area postrema* section of the 2-month *Nxnl2*$^{+/+}$ mouse.

preoptic nucleus receive afferents from the subfornical organ.

The expression of *Nxnl2* is circumscribed, but not restricted, to regions of the brain that are permeable to blood-borne molecules such as circulating hormones. The proximity of the *Nxnl2* expressing cells in the *area postrema* to microvascular can be appreciated by immunohistochemistry using antibody against plasmalemma vesicle-associated protein (PLVAP/MECA-32) (Fig. 3C). MECA-32 is expressed in central and peripheral vasculature throughout development, but its expression in the cerebrovasculature is downregulated upon the establishment of the blood-brain barrier in the adult, remaining only expressed in vascular endothelial cells that establish fenestrated capillaries [48]. By RT-PCR, we show that the mRNA of both products of the *Nxnl2* gene, the trophic factor RdCVF2 and the thioredoxin-related protein RdCVF2L are expressed by cells of the *area postrema* of the *Nxnl2*$^{+/+}$ mouse and confirm the absence of RdCVF2 and RdCVF2L mRNAs in the homozygous *Nxnl2*$^{R/R}$ mouse (Fig. 3D). Since RdCVF2 is secreted [1] and because the action of its paralogue, RdCVF, is relayed by the glucose transporter GLUT1 [7], we looked at the expression of GLUT1 in the *area postrema* of the *Nxnl2*$^{+/+}$ mouse. The expression of GLUT1 excluded a local role of GLUT1 in the potential protective action of RdCVF2) (Fig. 3E) [49].

2.4. Impaired metabolism of hippocampal specimens of *Nxnl2*$^{-/-}$ mice

In rodents, the *area postrema* is a single structure that descends out in to the 4th ventricle. By its position, even in the presence of an ependymal layer along the ventricular walls of the *area postrema*, the signals generated in the *area postrema* could circulate in the CSF to reach the brain areas that participate in the complex behavioral syndrome of the *Nxnl2*$^{-/-}$ mouse. The absence of suitable RdCVF2 antibodies led us to test this hypothesis by quantifying the metabolism of the hippocampus, since the paralog RdCVF in the retina regulates retinal metabolism. We standardized the dissection of well-mapped hippocampal specimens of 2 mm in diameter and 0.5 mm in thickness (Fig. 4A). The concentration of 39 metabolites covering 11 metabolic pathways was quantified in quadruplicates pools made of three standard specimens of the hippocampus of 2-month *Nxnl2*$^{+/+}$ and *Nxnl2*$^{-/-}$ mice, for two successive experiments using slightly different metabolomic technologies (Table 1). Focusing here on differences in concentrations that are statistically significant for the first experiment, we organized the results centering on glucose consumption, as it is the major source of energy for neurons. The concentration of glucose-1-phosphate, a metabolite of glycogenolysis that corresponds to the production of glucose-6-phosphate (G6P) from glycogen storage, is lower in hippocampus specimens of *Nxnl2*$^{-/-}$ mice (Fig. 4B). Mice lacking glycogen synthase, essential for glycogen production, have impaired hippocampal LTP, similar to *Nxnl2*$^{-/-}$ mice [50]. The concentration of three metabolites of glycolysis: G6P, fructose 1,6-bisphosphate (FBP) and 2/3-phosphoglycerate (2/3 PG) is higher in hippocampus specimens of *Nxnl2*$^{-/-}$ than that of *Nxnl2*$^{+/+}$ mice (Fig. 4C). The concentration of UDP-N-acetylglucosamine is lower in *Nxnl2*$^{-/-}$ hippocampus specimens (Fig. 4D). This metabolite is involved in O-GlcNAcylation of targeted proteins and produced by the hexosamine pathway that branches from glycolysis at the level of fructose-6-phosphate (F6P) [51]. O-GlcNAcylation of hippocampal proteins is reduced in brain starving of glucose, which decreases neuronal O-GlcNAcylation level in the hippocampus, impairs cognition and reduces dendritic spine density in the hippocampus of adult mice [52]. The concentration of phosphoribosylpyrophosphate, produced by the PPP is also lower in *Nxnl2*$^{-/-}$ hippocampal specimens (Fig. 4E). Collectively, the results represent an increase in the concentration of glycolytic metabolites and a decrease in that of glycogenolysis, hexosamine pathway and PPP (Fig. 4F). The concentrations of variable glycolytic metabolites are correlated, such as G6P with 2/3 PG ($r = 0.7372$, $p = 0.0150$, $n = 10$) and with FBP (Supl. Fig. 4A). In order to test the robustness of these data, we repeated the experiment with an additional cohort using an Orbitrap, a more precise instrument (Table 1) [53]. The additional results confirm the elevated concentration of the three identified glycolytic metabolites in the *Nxnl2*$^{-/-}$ hippocampal specimens and reveal a fourth one, phosphoenolpyruvate (Supl. Fig. 4B and C). Since both experiments include an internal standard, we combined their results, revealing that the lower concentration of UDP-N-acetylglucosamine in the *Nxnl2*$^{-/-}$ specimens is associated with an increase of UDP in the hexosamine pathway, two phenomena possibly linked metabolically (Supl. Fig. 4D) [54]. We found a slight but significant difference between the two experiments by analyzing the ratio ADP/ATP, but that small difference does not modify the general interpretation of the results (Supl. Fig. 4E) [55].

The steady-state concentration of a metabolite is proportional to its enzymatic production and use by the following metabolic reaction. It is consequently impossible to ensure that the increase in the concentration of G6P, as it is a central metabolite in different metabolic pathways, result from a higher rate of its synthesis by hexokinase or a reduced rate of entry into PPP, glycogen synthesis or glycolysis [51]. Since the conversion of glucose to G6P is irreversible, the production of G6P from glucose is directly linked to intercellular glucose that is uptaken by cells of the central nervous system by facilitative diffusion glucose transporters of the SLC2A family. We analyzed the expression of the three major SLC2A glucose transporters, GLUT1, GLUT3 and GLUT4 in the standard specimens of the hippocampus by western blotting. The expression of GLUT1 was found to be equivalent for both genotypes (Fig. 4G and Supl. Fig. 4F). A similar observation was made for GLUT3 (Supl. Fig. 4G). Four of the bands detected are specific (Supl. Fig. 4H). We detected two isoforms of the insulin-responsive glucose transporter GLUT4, the full-length isoform migrating above 50 kDa and a second isoform, most likely a non-functional GLUT4 protein (ΔEx-3-5) resulting from alternative splicing (Fig. 4H) [56]. The expression of the functional and full-length isoform is specifically reduced in the hippocampal specimens of *Nxnl2*$^{-/-}$ mice, which could contribute to the deficit in learning and memory of these mice since insulin modulates hippocampus-mediated spatial working memory via GLUT4 (Fig. 4I) [57]. The expression of glucose transporters and levels of metabolized analyzed by metabolomics suggests that the accumulation of glycolytic metabolites in the *Nxnl2*$^{-/-}$ hippocampus results in the deceleration of the metabolic flux triggering metabolite accumulation, captured at the time of the sacrifice of the animals.

2.5. The synergistic action of RdCVF2 and RdCVF2L in repairing the hippocampal dysfunction of *Nxnl2*$^{-/-}$ mice

The *Nxnl2*$^{-/-}$ hippocampus metabolic profiling supports that by analogy to RdCVF, produced by rods to stimulates cone metabolism in the retina [13], RdCVF2 produced in the *area postrema* increases glycolysis in cells within the hippocampus. In order to test this hypothesis, we constructed self-complementary adeno-associated vectors (AAV) encoding for RdCVF2 or RdCVF2L and GFP via a self-cleaving 2A peptide under the control of the cytomegalovirus enhancer/chicken β-actin (CMV/CBA) promoter. Serotype 9 allows AAV vectors to penetrate the brain when injected into the bloodstream of neonatal mice before the establishment of the blood-brain barrier [7,58]. In order to account for the purity and the functional titer of the AAV particles, we characterized the viral preparations with silver stain gel and electron microscopy. The silver stain showed no major impurities other than the VP1-3 proteins in expected ratios (Supl. Fig. 5A). The percentage of empty capsid particles of these preparations was quantified by transmission electron microscopy after uranyl acetate staining (Supl. Fig. 5B). While, the negative control (AAV2/9-GFP) has a ratio empty/total distinct from the two other recombinant AAVs, these two preparations have an indistinguishable ratio.

Following the intracardiac injection of *Nxnl2*$^{-/-}$ ♂ mice at post-natal day (PN) 4, the distribution of the transgene in the brain at 2 months was examined using anti-GFP immunohistochemistry (Fig. 5A). Among the cells transduced by AAV2/9.2 YF-CMV/CBA-RdCVF2^{2A}GFP the

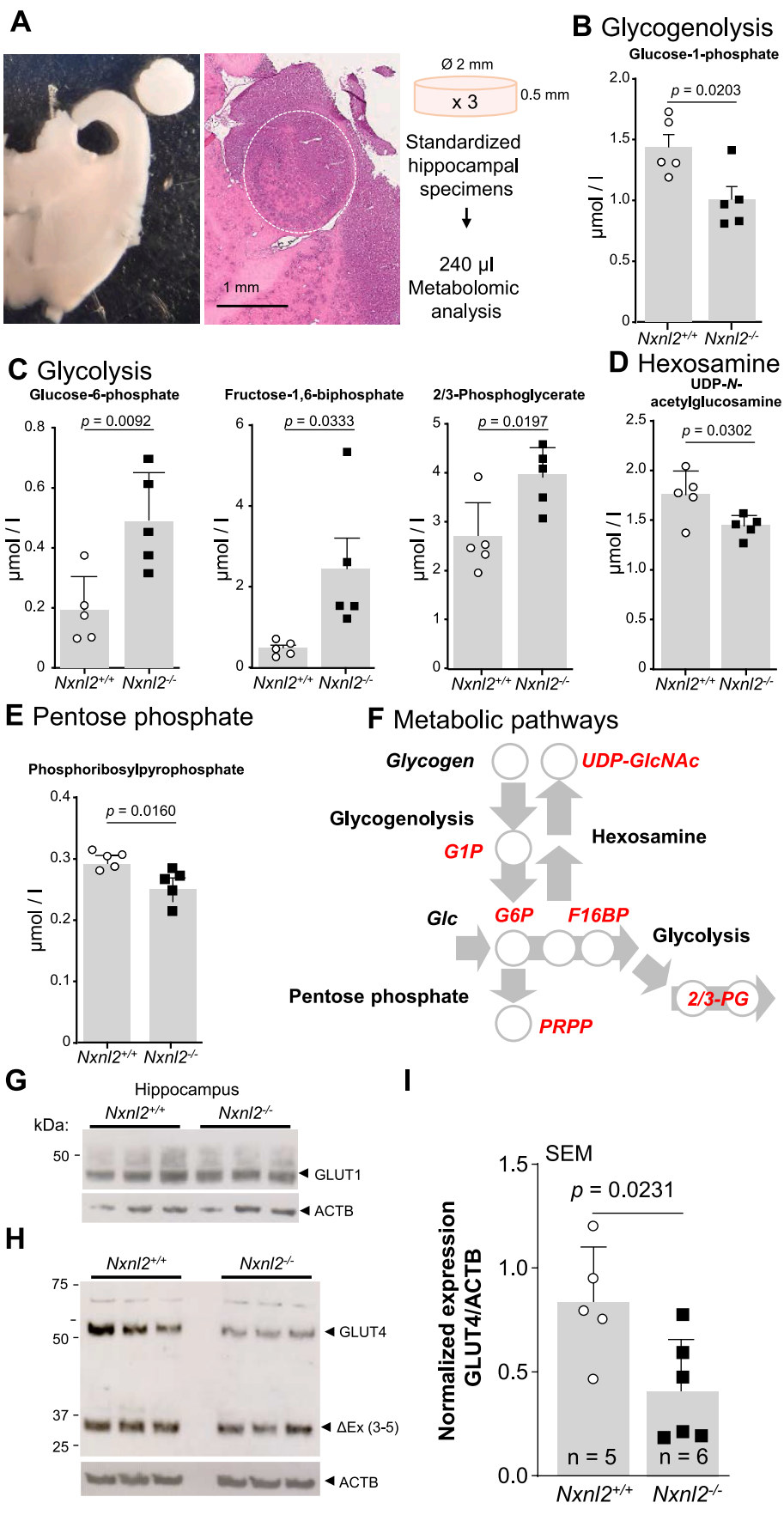

Fig. 4. Metabolomic analysis of hippocampal standardized specimens of *Nxnl2*$^{-/-}$ mice. (A) Representative pictures of a standardized specimen of the hippocampus. Left, bright-field microscopy and right hematoxylin and eosin staining. The white dotted circle delineates the surface of the hippocampal specimen. (B–F) Metabolomic analysis of the hippocampus specimens of 2-month ♂ mice. (B) Glycogenolysis. (C) Glycolysis. (D) Hexosamine pathway (E) Pentose phosphate pathway. (F) Metabolic pathways. 2/3-PG: 2/3-phosphoglycerate, F16BP: fructose-1,6-biphosphate, G1P: glucose-1-phosphate, G6P: glucose-6-phosphate, PRPP: phosphoribosylpyrophosphate and UDP-GlcNAc: UDP-N- acetylglucosamine. (G) Expression GLUT1 (SLC2A1) in the hippocampus specimens of 2-months ♂ mice. (H) Expression GLUT4 (SLC2A4) in the hippocampus specimens of 2-months ♂ mice. The invariant band ΔEx (3–5) is most likely a splicing variant previously reported. I) Quantification of the expression of GLUT4 in the hippocampus specimens of 2-months ♂ mice. The data are plotted with SEM. The data were analyzed by t-tests using GraphPad.

Table 1
Metabolomic analysis of hippocampal standardized specimens of *Nxnl2*$^{-/-}$ mice.
Summary of two experiments performed with hippocampus specimens of 2-months ♂ mice, using either quadrupole-trap (Qtrap) or an orbitrap. The concentration of metabolites sorted by their metabolic pathway are expressed in μM (μmol/l) in 240 μl of extraction solution corresponding to three standardized hippocampal specimens from individual mice. For concentration that are above the standard curve, the concentration is expressed as a ratio of carbon isotopes $^{12}C/^{13}C$ (C12/C13), the later isotope coming from the internal standard (IDMS), added before the extraction of the metabolites.[1] Limit of quantification,[2] n = 4: one outlier rejected using Grubs method,[3] Not quantified,[4] Not detected.

Study ID	Metabolite	First experiment (Qtrap)		Second experiment (Orbitrap)		Metabolic pathway
		Nxnl2$^{+/+}$ ($n = 5$)	*Nxnl2*$^{-/-}$ ($n = 5$)	*Nxnl2*$^{+/+}$ ($n = 5$)	*Nxnl2*$^{-/-}$ ($n = 4$)	
1	UDP-Glucose (μmol/l)	2.32 ± 0.54	2.43 ± 0.55	2.70 ± 0.20	2.81 ± 0.53	Glycogen synthesis
2	Glucose-1-phosphate (μmol/l)	1.43 ± 0.23	0.99 ± 0.24	1.63 ± 0.30	3.34 ± 1.34	Glycogenolysis
3	Glucose-6-phosphate (μmol/l)	0.19 ± 0.11	0.49 ± 0.16	0.16 ± 0.03	0.26 ± 0.08	Glycolysis
4	Fructose-6-phosphate (F6P) (μmol/l)	0.06 ± 0.06	0.25 ± 0.11	0.35 ± 0.03	0.37 ± 0.05	Glycolysis
5	Mannose-6-phosphate (μmol/l)	0.03 ± 0.03	0.11 ± 0.09	0.10 ± 0.01	0.11 ± 0.01	Hexosamine pathway (branching on F6P)
6	UDP-*N*-acetyl-glucosamine (μmol/l)	1.76 ± 0.24	1.45 ± 0.11	1.55 ± 0.19	1.35 ± 0.20	Hexosamine pathway
7	GDP-mannose (μmol/l)	0.45 ± 0.14	0.31 ± 0.05	LOQ	LOQ[1]	Hexosamine pathway
8	Fructose-1,6-biphosphate (μmol/l)	0.48 ± 0.18	2.45 ± 1.70	0.34 ± 0.11	1.18 ± 0.53	Glycolysis
9	Glycerol-3-phosphate (C12/C13)	2.29 ± 0.29	2.58 ± 0.33	5.41 ± 0.73	7.05 ± 1.68	Kennedy path. (branching on glycolysis)
10	2/3-Phosphoglycerate (2/3-PG) (μmol/l)	2.70 ± 0.75	3.97 ± 0.62	1.35 ± 0.19	2.30 ± 1.12	Glycolysis
11	Phospho-serine (μmol/l)	0.05 ± 0.01	0.06 ± 0.01	0.20 ± 0.01	0.23 ± 0.01	Serine synthesis (branching on 3-PG)
12	Phosphoenolpyruvate (μmol/l)	0.65 ± 0.26	0.77 ± 0.16	0.47 ± 0.05	0.83 ± 0.41	Glycolysis
13	Citrate (C12/C13)	0.57 ± 0.11	0.54 ± 0.08	0.48 ± 0.03	0.39 ± 0.05	Tricarboxylic acid cycle
14	*cis*-Aconitate (μmol/l)	0.44 ± 0.05	0.43 ± 0.11	0.33 ± 0.02	0.29 ± 0.03	Tricarboxylic acid cycle
15	α-Ketoglutarate (C12/C13)	2.62 ± 0.08	2.57 ± 0.28	2.96 ± 0.20	3.16 ± 0.51	Tricarboxylic acid cycle
16	2-Hydroxyglutarate (μmol/l)	0.60 ± 0.08	0.63 ± 0.16	0.67 ± 0.05	0.68 ± 0.11	Branching from α-Ketoglutarate
17	Succinate (C12/C13)	0.20 ± 0.11	0.14 ± 0.05	0.24 ± 0.08	0.41 ± 0.09	Tricarboxylic acid cycle
18	Fumarate (C12/C13)	5.83 ± 1.73	5.93 ± 0.83	4.42 ± 0.29	3.78 ± 0.76	Tricarboxylic acid cycle
19	Malate (C12/C13)	6.83 ± 0.95	6.79 ± 1.03	4.59 ± 0.29	4.27 ± 0.73	Tricarboxylic acid cycle
20	6-Phosphogluconate (μmol/l)	0.07 ± 0.03	0.11 ± 0.05	0.17 ± 0.02	0.50 ± 0.21	Pentose phosphate pathway
21	Ribose-1-phosphate (μmol/l)	24.9 ± 3.3	22.0 ± 0.8	8.02 ± 0.94	6.35 ± 0.33	Pentose phosphate pathway
22	Ribose-5-P + Ribulose-5-P (μmol/l)	4.28 ± 0.93	5.03 ± 1.28	2.97 ± 0.21	1.72 ± 0.47	Pentose phosphate pathway
23	Rib-5P (μmol/l)	NQ	NQ[3]	2.97 ± 0.21	1.72 ± 0.47	Pentose phosphate pathway
24	Ribulose-5P (μmol/l)	NQ[3]	NQ[3]	2.40 ± 0.10	1.38 ± 0.37	Pentose phosphate pathway
25	Phosphoribosyl diphosphate (μmol/l)	0.29 ± 0.01	0.25 ± 0.03	0.27 ± 0.02	0.28 ± 0.04	Pentose phosphate pathway
26	Sedoheptulose-7-phosphate (μmol/l)	1.60 ± 0.50	1.60 ± 040	LOQ[1]	LOQ[1]	Pentose phosphate pathway
27	AMP (μmol/l)	3.92 ± 0.42	3.86 ± 0.66	2.82 ± 0.17	3.74 ± 0.86	Nucleotides synthesis
28	ADP (C12/C13)	10.4 ± 1.0	10.4 ± 2.3	10.0 ± 0.80	11.4 ± 2.8	Nucleotides synthesis
29	ATP (C12/C13)	8.84 ± 0.79	8.91 ± 1.87	9.55 ± 0.87	11.3 ± 3.6	Nucleotides synthesis and OXPHO
30	CMP (μmol/l)	0.34 ± 0.04	0.31 ± 0.06	0.72 ± 0.09	0.79 ± 0.21	Nucleotides synthesis
31	CDP (μmol/l)	0.11 ± 0.02	0.11 ± 0.01	0.17 ± 0.01	0.24 ± 0.08	Nucleotides synthesis
32	CTP (μmol/l)	0.04 ± 0.02	0.03 ± 0.01	LOQ[1]	LOQ[1]	Nucleotides synthesis
33	GMP (μmol/l)	1.22 ± 0.15	1.07 ± 0.17	0.93 ± 0.10	1.15 ± 0.21	Nucleotides synthesis
34	cGMP (μmol/l)	0.23 ± 0.03	0.17 ± 0.06	ND[4]	ND[4]	Nucleotides synthesis
35	GDP (μmol/l)	2.73 ± 0.49	3.64 ± 0.91	2.26 ± 0.30	2.53 ± 0.92	Nucleotides synthesis
36	Orotate (μmol/l)	0.03 ± 0.03	0.11 ± 0.09	0.09 ± 0,01	0.10 ± 0.01	Nucleotides synthesis
37	UMP (μmol/l)	2.38 ± 0.26	2.40 +/0.30	2.83 ± 0.19	3.02 ± 0.57	Nucleotides synthesis
38	UDP (μmol/l)	0.31 ± 0.05	0.36 ± 0.11	0.16 ± 0.03	0.36 ± 0.21	Nucleotides synthesis
39	UTP (μmol/l)	0.37 ± 0.12	0.31 ± 0.08	0.09 ± 0.01	0.11 ± 0.03	Nucleotides synthesis

pyramidal neurons of the hippocampus are predominant (Fig. 5B). This peculiar tropism is not dependent on the encoded sequence since it was also observed for AAV2/9.2 YF-CMV/CBA-RdCVF2L^{2A}GFP, as seen in a previous study (Supl. Fig. 5C) [59].

CA1 basal synaptic transmission of the *Nxnl2*$^{-/-}$ hippocampus is slightly higher than that of *Nxnl2*$^{+/+}$ at two months after administration of the negative control (Supl. Fig. 5D). A similar observation was made for the two other vectors delivered individually or in combination (Supl. Fig. 5E). Nevertheless, no difference in the CA1 basal synaptic transmission could be observed between *Nxnl2*$^{-/-}$ at 2 months after delivery of RdCVF2 or RdCVF2L encoding AAVs (Supl. Fig. 5F). For measuring LTP, we proceeded as previously except that we recorded only one hippocampal slice per mouse to assure sphericity, which permits the use of two-way ANOVA - repeated measures for the statistical analysis of the results. In repeat measure design, each animal receives one of the treatments and then is measured at specific time points. Hence, animals are the experimental units [60]. In this new configuration, the treated mice are compared in a preclinical setting [61]. At two months, the traces of post-high frequency stimulation (HSF) recordings show an alteration for *Nxnl2*$^{-/-}$ versus *Nxnl2*$^{+/+}$ hippocampus after AAV-GFP injection and intermediate situation for the *Nxnl2*$^{-/-}$ mice injected with *Nxnl2* gene products (Fig. 5C). RdCVF2 alone rescues partially but significantly the fEPSP response of the *Nxnl2*$^{-/-}$ hippocampus when compared to AAV-GFP, supporting the formulated hypothesis above (Fig. 5D). Interestingly, we observed the same partial correction after the injection of AAV-RdCVF2L (Fig. 5E). More importantly, the combined administration of half the dose of RdCVF2 and RdCVF2L results in an almost complete reversion of LTP deficit of *Nxnl2*$^{-/-}$ mice at 2 months (Fig. 5F). This indicates that both products of the *Nxnl2* gene act synergistically to restore the altered function of the hippocampus of the *Nxnl2*$^{-/-}$ mouse. The statistical power of repeat measure design is well illustrated by comparison to the design used in Fig. 2 (Supl. Fig. 5G). A close view of the fEPSP measures immediately following the HSP reveals a distinct recording traces that may be related to two different but coordinated rescue mechanisms (Supl. Fig. 5H). Following our hypothesis, the non-cell-autonomous activity of RdCVF2 does not require that AAV-RdCVF2 targets any specific region of the brain. However, the presumably cell-autonomous action of the thioredoxin-related protein RdCVF2L requires the transduction of dysfunctional cells, most likely, the hippocampal pyramidal neurons (Supl. Fig. 5C).

We analyzed the effect of the corrective therapy on cellular metabolism using 2-month hippocampal specimens (Supl. Fig. 6A). Overall,

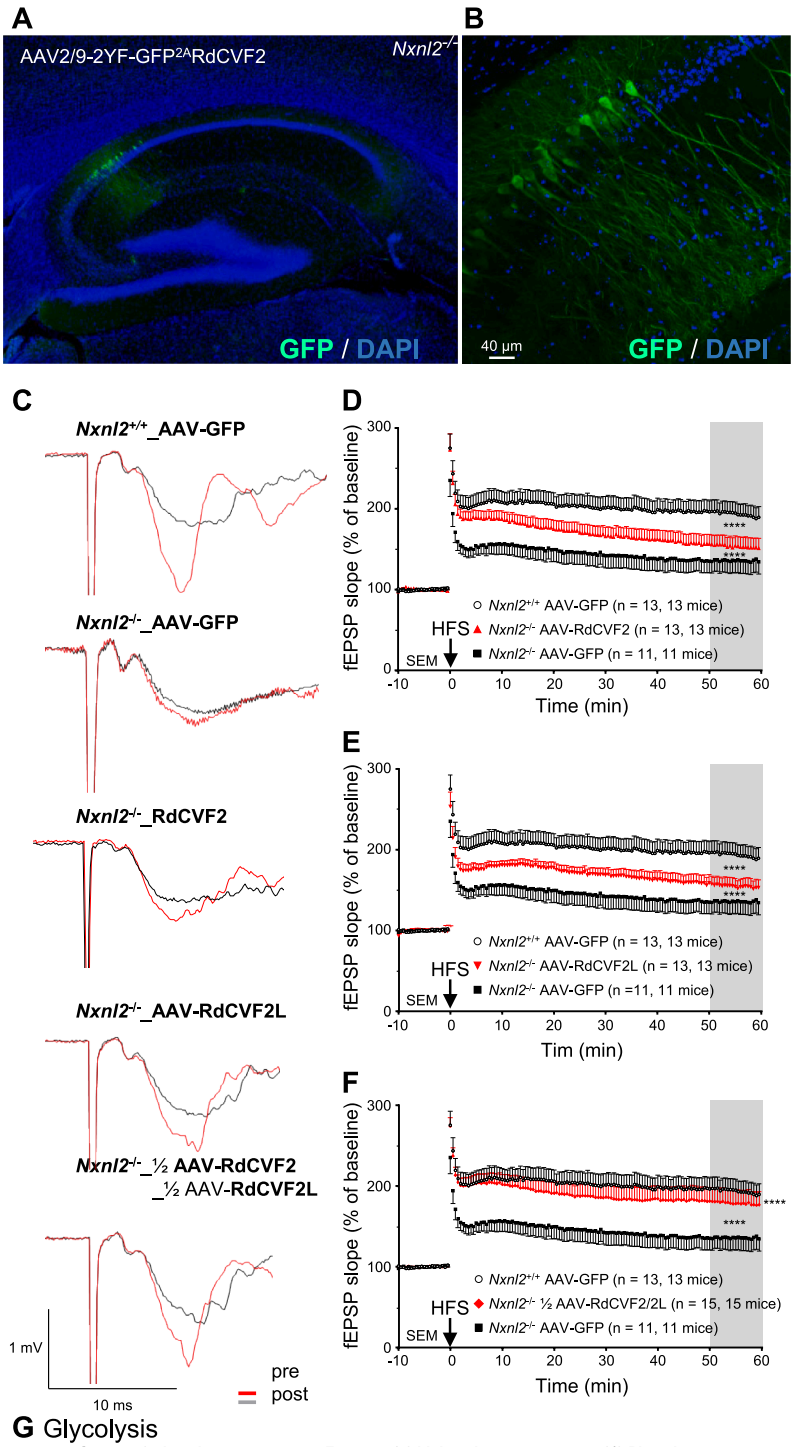

Fig. 5. Treatment of the *Nxnl2*$^{-/-}$ mouse with recombinant AAVs encoding RdCVF2 and RdCVF2L. (A) Representative image of the expression of GFP detected by immunohistochemistry in the brain of 2-months ♂ *Nxnl2*$^{-/-}$ mice injected with AAV2/9-2 YF-CMV/CBA-RdCVF2^{2A}GFP. (B) Higher magnification displaying the transduced hippocampal pyramidal neurons. (C) Representative traces of the pre- and post-HFS recording on hippocampal slices from ♂ mice aged of two months. (D) Normalized CA3-CA1 fEPSPs mean slope recorded from 2-month-old *Nxnl2*$^{+/+}$ and *Nxnl2*$^{-/-}$ mice injected with AAV2/9-2 YF-CMV/CBA-GFP and from age-matched *Nxnl2*$^{-/-}$ mice injected with AAV2/9-2 YF-CMV/CBA-RdCVF2^{2A}GFP. A high frequency stimulation train was delivered (arrow) following a 10 min baseline. (E) Normalized CA3-CA1 fEPSPs mean slope recorded from 2-month-old *Nxnl2*$^{+/+}$ and *Nxnl2*$^{-/-}$ mice injected with AAV2/9-2 YF-CMV/CBA-GFP and from age-matched *Nxnl2*$^{-/-}$ mice injected with AAV2/9-2 YF-CMV/CBA-RdCVF2L^{2A}GFP. A high frequency stimulation train was delivered (arrow) following a 10 min baseline (F) Normalized CA3-CA1 fEPSPs mean slope recorded from 2-month-old *Nxnl2*$^{+/+}$ and *Nxnl2*$^{-/-}$ mice injected with AAV2/9-2 YF-CMV/CBA-GFP and from age-matched *Nxnl2*$^{-/-}$ mice injected with half the dose used previously (½) of AAV2/9-2 YF-CMV/CBA-RdCVF2^{2A}GFP combined with ½ of AAV2/9-2 YF-CMV/CBA-RdCVF2L^{2A}GFP. A high frequency stimulation train was delivered (arrow) following a 10 min baseline (G) Metabolomic analysis of *Nxnl2*$^{-/-}$ mice at 2-month injected with AAV2/9-2 YF-CMV/CBA-GFP or with ½ AAV2/9-2 YF-CMV/CBA-RdCVF2^{2A}GFP + ½ of AAV2/9-2 YF-CMV/CBA-RdCVF2L^{2A}GFP. The data are plotted with SEM. The LTP data were analyzed using two-way ANOVA - repeated measures. The metabolomic data were analyzed using one-way ANOVA.

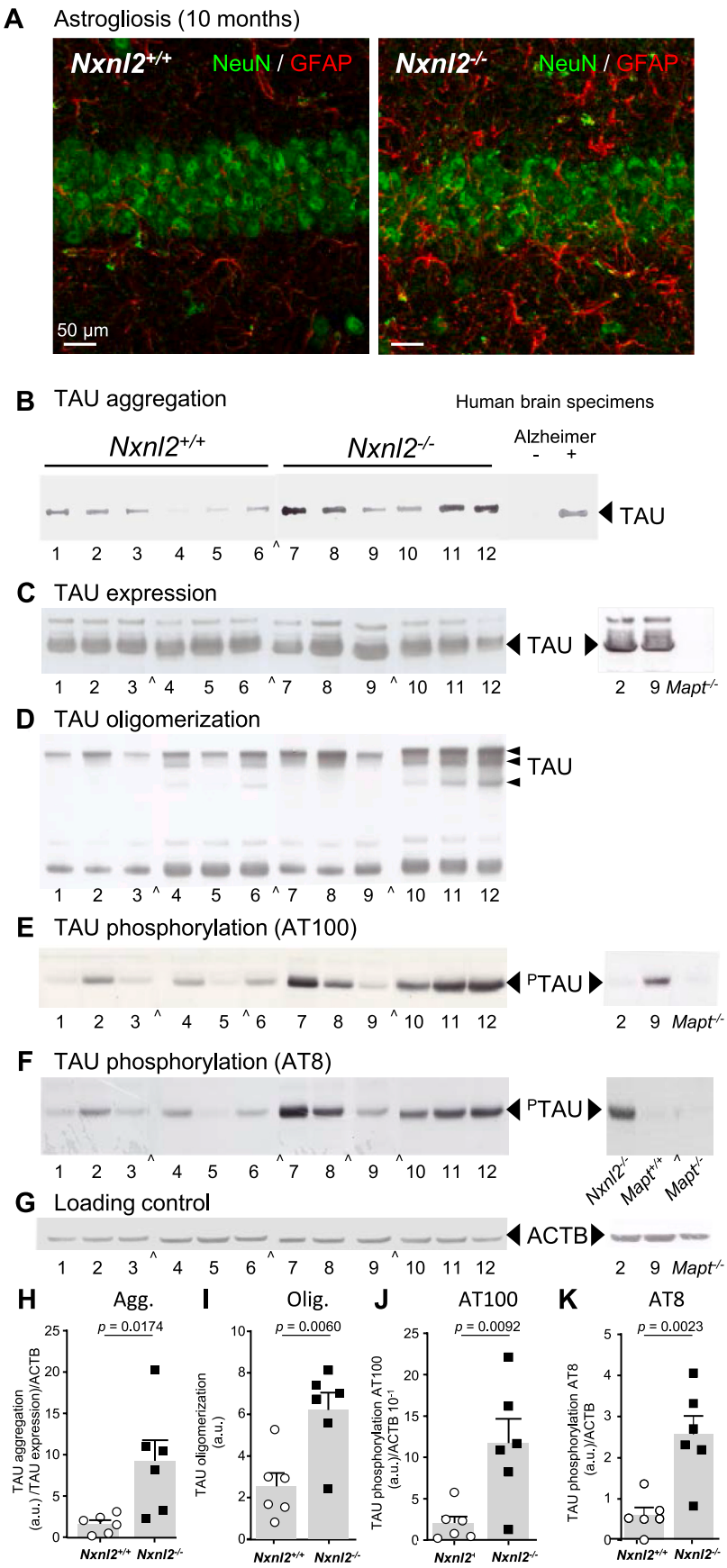

Fig. 6. Analysis of astrogliosis in the brain of *Nxnl2*$^{-/-}$ at 10 months of age using immunohistochemistry and TAU status by 18 months of age using biochemical methods. (A) Immunohistochemical analysis of the expression of glial fibrillary acidic protein (GFAP) in the hippocampus of 10 months aged ♂ mice. The neurons are visualized through the expression of the neuronal marker RNA binding protein fox-1 homolog 3 (RBFOX3/NeuN). (B) TAU aggregation using whole brain extracts after removing of the cerebellum of 18 months aged ♂ mice. The brain extracts of the right are that of human brain from aged-matched healthy and Alzheimer persons scored positive (+) and negative (−) for NFT. (C) TAU expression. On the right brain extracts from *Mapt*$^{-/-}$ ♂ mouse (C57BL/6-N background) at 18 months aged. (D) TAU expression analyzed by non-reducing gel electrophoresis. (E) TAU phosphorylation using AT100 antibody. On the right brain extracts from *Mapt*−/− ♂ mouse at 18 months aged. (F) TAU phosphorylation using AT8 antibody. On the right brain extracts from *Mapt*$^{t-/-}$ ♂ mouse at 18 months aged. (G) Loading control using cytoplasmic actin (ACTB) antibody. (H) Quantification of TAU aggregation normalized to TAU expression and to ACTB. (I) Quantification of TAU oligomerization. (J) Quantification of TAU phosphorylation using AT100 antibody normalized to ACTB. (K) Quantification of TAU phosphorylation using AT8 antibody normalized to ACTB. The data are plotted with SEM. The data were analyzed using t-tests.

the intracardiac injection of AAV does not modify the metabolism within the hippocampus, since the concentrations of metabolites are equivalent in *Nxnl2*$^{+/+}$ and *Nxnl2*$^{-/-}$ mice injected with AAV-GFP to those without injection (Table 1). The three glycolytic metabolites (G6P, FBP and 2/3 PG) are elevated in the *Nxnl2*$^{-/-}$ specimens after injection of either AAV-GFP or ½ AAV-RdCVF2 + ½ AAV-RdCVF2L (Fig. 5G). As previously observed, the concentration of G6P and FBP are correlated (Supl. Fig. 6B). The glycogenolysis and the hexosamine pathway (Supl. Fig. 6B, D) do not seem to be modified. Surprisingly the PPP was affected, as previously but was not corrected by the products of the *Nxnl2* gene (Supl. Fig. 6E). We could not identify any metabolite that correlates statistically with the corrective effect measured by electrophysiology. We have used in that experiment animals of both sexes, but this is not the reason for the lack of effect on the metabolism (Supl. Fig. 6A). Pyramidal neurons that generate LTP represent a subset of the cell population and even possibly involve only a subset of synapses drowned in the mass of the hippocampus specimens [62]. This situation may preclude the identification to any significant change in metabolite concentration in the hippocampus as a whole. We validated the transduction of the AAVs expression of GFP in these specimens (Supl. Fig. 5I). We also analyzed the level of expression of GLUT4 in hippocampal specimens after AAV delivery. The treatment did not restore GLUT4 expression, but the result can be interpreted as a trend (Supl. Fig. 5J). This observation may be explained by the fact that only a subset of cells expresses GLUT4, among which the pyramidal neurons [63].

2.6. *TAU is aggregated in the brain of the Nxnl2*$^{-/-}$ *mouse at 18 months of age*

The contribution of RdCVF2L in the reversion of deficit in LTP was explored in the light of its ability to prevent TAU phosphorylation [3]. TAU phosphorylation favors its aggregation leading to the formation of NFT. At 2 months, the absence of difference in the status of TAU phosphorylation in the brain of *Nxnl2*$^{-/-}$ versus *Nxnl2*$^{+/+}$ mice rules out the idea that LTP deficit of the *Nxnl2*$^{-/-}$ mice is produced by interference of TAU phosphorylation. (Supl. Fig. 7AB). In order to study TAU aggregation, we standardized a filter binding assay with human brain specimens of Braak stage VI [64] (Alzheimer +) and age-matched non Alzheimer brain (Alzheimer -) (Supl. Fig. 7C). NFT are characteristic of in Braak stage VI as detected by Gallyas-silver iodide staining [65]. Using this quantitative assay, we found that the brain of 2-month *Nxnl2*$^{-/-}$ mice contain more aggregated TAU than the 2-month *Nxnl2*$^{+/+}$ brain (Supl. Fig. 7D). We found no difference in the expression of glial fibrillary acidic protein (GFAP) in the brain of 2-month mice (Supl. Fig. 7E), but discovered that the brain of the *Nxnl2*$^{-/-}$ mice show signs of neuroinflammatory astrogliosis at 10 months (Fig. 6A). The quantification of GFAP-positive cells in the CA1 region of the hippocampus at 12 months confirms the neuroinflammation (Supl. Fig. 7F). The upregulation of GFAP is likely preceded by the polarization of microglia (resident macrophages) that would aggravated hippocampal dysfunction by reducing glucose availability for neurons, as activated microglial cells shift towards glycolysis during inflammation [66]. Consequently, LTP deficit at 2 months does not result from neuroinflammatory astrogliosis (Supl. Fig. 7E), but may involve TAU aggregation (Supl. Fig. 7D).

By 18 months of age, TAU aggregation was found to be elevated in the brain of the *Nxnl2*$^{-/-}$ mice using filter finding assay on the whole brain (Fig. 6B and H). Human brain specimens from age-matched patients without and with NFT observed by anatomical pathology validate the assay (Supl. Fig. 7C). The expression of TAU protein is not modified in these conditions (Fig. 6C and G). The absence of expression of TAU in the brain specimen of the *Mapt*$^{-/-}$ mouse demonstrates that the signal detected by western blotting is specific [67]. TAU oligomers were more abundant in the brain of *Nxnl2*$^{-/-}$ mice (Fig. 6D and I). They are probably composed of phosphorylated TAU proteins, as seen in brain specimens of Alzheimer's disease patients. A growing body of evidence

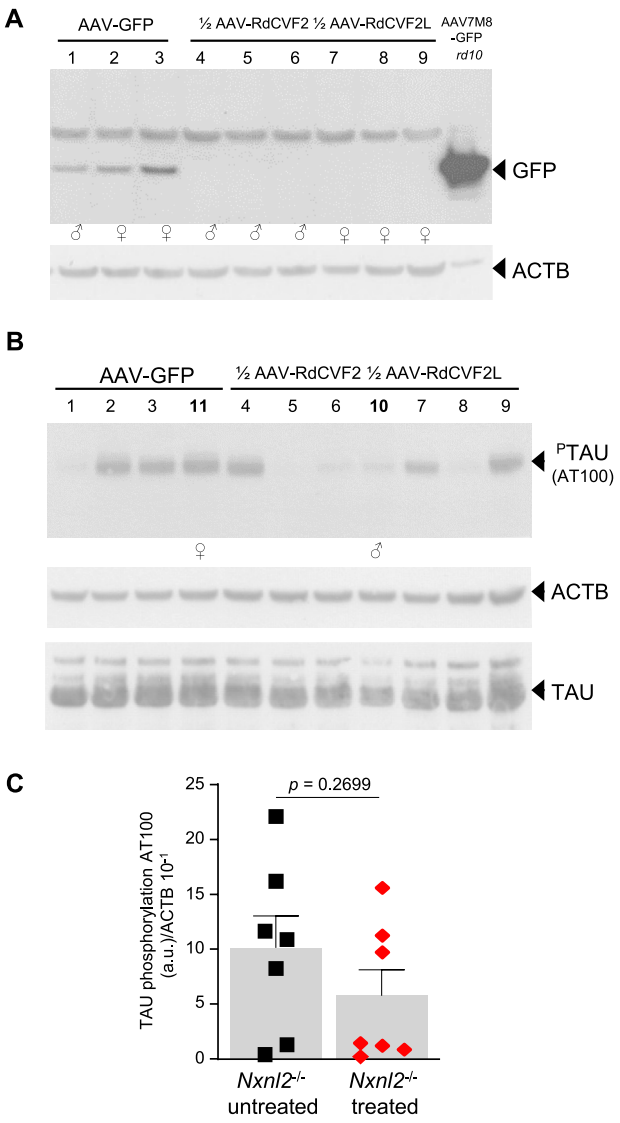

Fig. 7. Phosphorylation of TAU using AT100 antibody in the brain of treated 18-months *Nxnl2*$^{-/-}$ mice. (A) Expression of GFP in whole brain extracted of treated *Nxnl2*$^{-/-}$ mice at 18 months of age. The sex of the animals is indicated. (B) Phosphorylation of TAU using AT100 antibody in whole brain extracts of treated *Nxnl2*$^{-/-}$ mice at 18 months of age. The sex of additional *Nxnl2*$^{-/-}$ mice (10 and 11 in bold) is indicated. (C) Comparison of the level of phosphorylation of TAU using AT100 antibody in whole brain extracts of untreated 18-months *Nxnl2*$^{-/-}$ mice (Fig. 6J) to that of *Nxnl2*$^{-/-}$ mice at 18 months of age treated with ½ AAV2/9-2 YF-CMV/CBA-RdCVF2^{2A}GFP + ½ of AAV2/9-2 YF-CMV/CBA-RdCVF2L^{2A}GFP. Data were analyzed using one-way ANOVA.

indicates that TAU oligomer formation precedes the appearance of NFT and contributes to neuronal loss. Cysteines residues (C^{608} and C^{639}, P10636-1) within the regions R2 and R3 of the microtubule binding domain of TAU are involved in the formation of these oligomers of TAU. Phospho-TAU antibody AT100 is specific to the phosphorylated TAU at f T^{529}, S^{531} and T^{534}, AT8 recognizes Ser^{519} and T^{522} (P10636-1). The sequence surrounding these phosphorylated residues encompasses 45 amino-acids region that is 100% identical between human and mouse TAU (P10637-1). Those two well-studied epitopes are frequently found in postmortem brain specimens of patients who died of Alzheimer's disease [68]. We found more phosphorylation using AT100 (Fig. 6E and J) and AT8 antibodies (Fig. 6F and K) in whole brain samples from *Nxnl2*$^{-/-}$ as compared to *Nxnl2*$^{+/+}$ mouse brains. We also found correlations of aggregation, oligomerization and phosphorylation. The correlation of aggregation with oligomerization (r = 0.6164, *p* =

0.0328) is lower than with phosphorylation at both AT100 ($r = 0.9406$, $p < 0.0001$) and AT8 ($r = 0.8889$, $p = 0.0001$) epitopes, suggesting that TAU oligomerization precedes its phosphorylation in the temporal sequence that leads to its aggregation within the *Nxnl2*$^{-/-}$ brain (Supl. Fig. 6G). Phosphorylation at AT8 and AT100 epitopes are highly correlated ($r = 0.9119$, $p < 0.0001$). We did not map the various stages leading from TAU oligomerization to its aggregation within the *Nxnl2*$^{-/-}$ brain. In Alzheimer's disease brains, the formation of NFT expands from the parahippocampal gyrus to the hippocampus and further to the cortex, so it is quite possible that the hippocampus of the *Nxnl2*$^{-/-}$ is affected by TAU aggregation as early as 2 months [38].

2.7. Prevention of TAU aggregation in the brain of the *Nxnl2*$^{-/-}$ mouse by 18 months' gene therapy

Nxnl2$^{-/-}$ mice got an intracardiac injection of recombinant AAV vectors at PN4, then housed in normal conditions for 18 months. Then, after sacrifice, the expression of the AAV transgene was analyzed by western blotting using 80 μg of whole brain extract with an anti-GFP antibody. As a positive control, we used a retinal extract of an *rd10* mouse subretinally injected with an AAV2-7M8-CMV/CBA-GFP [69]. We detected the expression of GFP in the brain of all *Nxnl2*$^{-/-}$ mice injected with AAV2/9-2 YF-CMV/CBA-GFP (Fig. 7A). However, we could not detect the expression of GFP in the brain of animals injected with ½ AAV2/9-2 YF-RdCVF2^{2A}GFP combined with ½ AAV2/9-2 YF-RdCVF2L^{2A}GFP. The absence of detectable GFP is likely reflective of the lower expression of GFP positioned downstream of a self-cleaving 2A peptide, as observed previously in the retina [7] (Supl. Fig. 5I), and the lower dose injected in this experiment (1×10^{12} vg) as compared to 4×10^{12} vg (Fig. 5). Bypassing this limitation, we measured semi-quantitatively the phosphorylation of TAU using AT100 antibody. The reduction of TAU phosphorylation in the whole brain of the *Nxnl2*$^{-/-}$ mice treated with both products of the *Nxnl2* gene is striking, even if it not statistically significant (Fig. 7B). There is a 20% reduction of the expression of TAU in those specimens, but this cannot explain the reduction of its phosphorylation. Since it has not been possible to visualize the expression of the transgenes, we do not know if mice 4 and 9 express the corrective genes. By excluding these two mice, 18% of the effective of the cohort, the difference in AT100 phosphorylation, standardized to the expression of TAU, grazes statistical significance ($p = 0.0719$). Excluding in addition mouse 1 that did not develop TAU phosphorylation for unknown reason, 27% of the cohort, the result becomes significant ($p = 0.0068$). This phenomenon is also visible if one takes into account the variability of AT100 phosphorylation observed in the untreated animals at 18 months (Fig. 6J). The average AT100 phosphorylation, normalized by cytoplasmic actin, is lower in the treated *Nxnl2*$^{-/-}$ mice (Fig. 7C). In other words, the treatment with the combination of RdCVF2 and RdCVF2L over 18 months-period reduces the phosphorylation, and by extension the aggregation of TAU, in five out of seven treated *Nxnl2*$^{-/-}$ mice.

3. Discussion

3.1. Possible mechanisms of the synergistic effect of RdCVF2 and RdCVF2L on hippocampal function

The *Nxnl2* gene is expressed in various parts of the mouse brain with a prominent expression in the *area postrema*, where both RdCVF2 and RdCVF2L are expressed. While we have not identified the types of cells that express the gene in this part of the brain, the *area postrema* is located at the interface of the blood circulation that carries peptidic hormones from the periphery to the central nervous system. In addition, the absence of brain blood barrier between this organ, as for other sensory circumventricular organs expressing *Nxnl2*, puts the gene at a node between circulating hormones regulating directly or indirectly glycemia, the concentration of circulating glucose and its use by neurons of the brain. The extracellular truncated trophic factor RdCVF2 can participate in the generation of LTP, recorded on hippocampal slices by acting on glucose uptake [1]. The *area postrema* is in contact with the CSF secreted by the choroid plexus. CSF circulation distributes glucose to cells of the brain through its regulated flow [70]. The absence of RdCVF2 is sensed by the abnormal glycolysis measured in the hippocampus of the *Nxnl2*$^{-/-}$ mouse (Fig. 4A–F). The restoration of LTP after delivery of RdCVF2 in this mouse model demonstrates the role of this truncated thioredoxin (Fig. 5D). To our surprise, we failed to restore the metabolism of the hippocampus by re-expressing the products of the *Nxnl2* gene under the control of a ubiquitous CMV/CBA promoter (Fig. 5G). We know that with this approach, RdCVF2 is expressed at abnormally higher levels in many cells in the brain, which is not a natural situation, regarding both its physiological distribution and its expression level [42]. This absence of correlation between function and metabolism means that the *Nxnl2* gene does not regulate glucose metabolism globally in the brain and that its effect is restricted to a subset of cells, and even a subset of cells in the hippocampus, such as pyramidal cells that generate the LTP in response to an excitatory signal. The modification of glycolysis in hippocampus is probably due to metabolic plasticity within the organ, such as astrocytes even if no GFAP reactivity could be observed at 2 months (Supl. Fig. 7E). The reintroduction of RdCVF2 under a ubiquitous promoter would not correct for this metabolic plasticity. GLUT4 expression is restricted by cells with altered function, and is downregulation in the *Nxnl2*$^{-/-}$ hippocampus is certainly involved (Fig. 4H) [63]. This fits with the regulation of glycolysis by RdCVF2 via its interaction with a cell-receptor expressed by the hippocampal pyramidal neurons as well as by other neurons involved in the other studied behaviors (Fig. 1). This putative cell surface receptor is certainly not BSG1 because its expression is restricted to the retina and the pineal gland [71]. We speculate that this receptor is complexed with GLUT4 by analogy with the mode of action of RdCVF, through GLUT1 [7].

The synergistic action of RdCVF2 with RdCVF2L is reminiscent of the action of its paralogue *Nxnl1*, involved in glucose uptake and in redox homeostasis in the retina [12,13]. A difference in the mode of action of RdCVF2 and RdCVF2L is reflected by non-contiguous fEPSP traces after gene therapy (Supl. Fig. 5H). Concerning redox homeostasis, the reduction of the concentration of one of the metabolites of the PPP in the first experiment is in agreement with such scenario (Fig. 4E). Nevertheless, one of the cysteines of the catalytic site of the thioredoxin-related protein RdCVF2 is replaced by a serine in all placental mammals for which the genome sequence is available [3]. Consequently, the RdCVF2L protein does not carry a thioredoxin active site, but that of a monothiol glutaredoxin, as glutaredoxin 3 [72]. Glutaredoxins reduce S-glutathionylation, of redox sensitive cysteines in proteins. Under oxidative stress conditions, cysteines are non-enzymatically oxidized with the tripeptide glutathione (GSH), one of the most crucial cellular thiol buffers. The formation of protein-SSG, termed S-glutathionylation, protects protein thiols under oxidative conditions, since it can be reverted by electron transfer. It prevents further oxidations of thiol groups of proteins to sulfenic, sulfinic, and sulfonic acids, the latter oxidation being irreversible. The protein S-glutathionylation cycle, initiated under oxidative conditions, is inverted when a reducing environment is restored. Deglutathionylation restores protein function and S-glutathionylated glutaredoxin is then reduced by reduced glutathione. Hippocampal-dependent learning and memory functions are peculiarly sensitive to oxidative stress [73]. The protection of LTP by RdCVF2L was achieved by direct transduction of hippocampal pyramidal neurons with AAV2/9-2 YF-RdCVF2L (Supl. Fig. 5C).

The positive role of the *Nxnl2* gene on synaptic plasticity and memory is theoretically produced by an effect on the N-methyl-D-aspartate (NMDA) receptors. Seven cysteines of NMDA-receptor subunits are regulated by oxidoreduction and could be targeted by the monothiol glutaredoxin activity of RdCVF2L [74]. The synergistic effect

of RdCVF2 and RdCVF2L would result from the action of RdCVF2 regulation of glucose metabolism on neurons of hippocampal pyramidal and by deglutathionylation of NMDA-receptor by RdCVF2L. Deglutathionylation of NMDA-receptor by RdCVF2L depends on metabolism of glucose by the PPP to generate NADPH and with RdCVF2 increasing glucose uptake, the action of RdCVF2L would be regulated by that of RdCVF2 [12].

RdCVF2 can also synergize with RdCVF2L by regulating transmembrane electrochemical gradients. The cellular Na/K-ATPase pump activity relies on ATP produced by glycolytic, rather than by ATP from mitochondrial respiratory chain [75]. The Na/K-ATPase re-establishes the potassium and sodium gradients which are necessary to fire action potentials. Neurons, such as hippocampal pyramidal neurons expend a large fraction of the ATP they produce to maintain their required intracellular Na and K concentrations [76]. RdCVF2 could increase locally, at the level of its receptor on hippocampal pyramidal neurons, the concentration of ATP produced from glucose by glycolysis. The addition of ATP generates functional LTP on hippocampal slices [77]. In addition, RdCVF2-mediated glycolysis can branch to the production of triglycerides that can participate in structural LTP, the reorganization of cytoskeletal architecture that produces new synaptic buttons, similarly to RdCVF's ability to stimulate aerobic glycolysis to produce of triglycerides for cone outer segment renewal [7]. A local action of RdCVF2 through the dendritic spines expressing its putative RdCVF2 cell-surface receptor and GLUT4 would explain the inability to restore the whole metabolism of the hippocampus (Fig. 5G) [63].

3.2. The implication of NXNL2 in neurodegenerative diseases

Oligomerization, phosphorylation at AT100 and AT8 epitopes and aggregation of TAU are hallmarks of tauopathies, such as Alzheimer's disease. Neuropathologically Alzheimer's disease is defined by the combined presence of extracellular amyloid-beta (Aβ) plaques and intracellular TAU NFT, but the *MAPT* gene encoding TAU was never found to be genetically associated with Alzheimer's disease [78]. Similar to *MAPT*, the *NXNL2* gene is not genetically associated with Alzheimer's disease [79]. This means that positive, but not negative genome wide association studies (GWAS) signals can lead to a conclusion on essential mechanisms of Alzheimer's disease and leaves opened the possibility of *NXNL2* participation in Alzheimer's disease.

There is growing evidence for a close link between altered glucose metabolism and Alzheimer's disease pathogenesis. Aging, viewed as a slow steady accumulation of unrepaired oxidative damages, is the most relevant risk factor triggering Alzheimer's disease as a disease-memory impairment of hippocampal function, the earliest affected brain region in Alzheimer's disease. Redox enzymes are candidate regulators of the disease. Due to its dual function in regulating glucose uptake and redox status of TAU, the *NXNL2* gene is positioned at a central place in this pathological aging scenario.

4. Conclusions

One of the most striking observations made on the *Nxnl2*$^{-/-}$ mouse model is the parallel between memory dysfunction at 2-months that resembles mild-cognitive impairment predisposing to the development of Alzheimer's disease [14] and the aggregation of TAU at 18-month, which is equivalent of NTF found in the brain of Alzheimer's disease patients, after autopsy. For the young *Nxnl2*$^{-/-}$ mouse, LTP dysfunction is attributed to the lack of RdCVF2 and RdCVF2L that act synergistically (Fig. 5A–F). For the aged *Nxnl2*$^{-/-}$ mouse, the protection against aggregation is believed to be the results of RdCVFL2 action, which can prevent TAU phosphorylation and its subsequent aggregation (Fig. 7) [3]. However, since the treatment was administrated in young animals, TAU aggregation may be the result of metabolic and redox dysfunctions that occurred progressively throughout the life of mice as shown in 2-month *Nxnl2*$^{-/-}$ brain (Supl. Fig. 7D). A highly speculative conclusion would be that treating patients at the stage of mild-cognitive impairment with the products of the *NXNL2* gene could be effective in preventing Alzheimer's disease. The restoration of LTP by corrective gene therapy shows this potential.

5. Experimental model and methods

5.1. See additional file 1 for complete methods

LTP recording

After delivery, Mice were housed in standard ventilated cages (IVC, Sealsafe, Techniplast, Marcoussis, France) coupled to an air-handling unit (TouchSLIMline, Exhaust, Techniplast, Marcoussis, France), equipped with solid floors and a layer of bedding. The cages were cleaned at regular intervals to maintain hygiene. Environmental parameters were as follows: temperature: ~22°C, relative humidity: ~55%. Mice had *ad libitum* access to standard rodent chow. The food was stored under dry and cool conditions in a well-ventilated storage room. Mice had *ad libitum* access to pre filtered and sterile water. The amounts of food and water were checked daily, supplied when necessary and refreshed once a week. Mice were kept on a 12-h light/dark cycle. Experimenters were blinded to genotype and treatment for all experiments. Data were analyzed by measuring the slope of individual fEPSPs at 0-1.5 ms from the top of the signal by linear fitting using Clampfit (Molecular Devices, Union City, CA). LTP was quantified by comparing the mean fEPSP slope over the post- high frequency stimulation (HFS) period with the mean fEPSP slope during the baseline period. Group effects was assessed by changes in fEPSP slope, expressed as the percentage of the baseline value. For figure 5, only one hippocampal slide was used per animals.

For the first experiment (Table 1), intracellular metabolites were analyzed as described in [17] Briefly, analysis was performed by high performance anion exchange chromatography (Dionex ICS 2000 system, Sunnyvale, USA) coupled to a triple quadrupole QTrap 4000 (AB Sciex, CA USA) mass spectrometer. This analytical technology allows the separation and analysis of numerous highly polar metabolites belonging to several chemical families in the same analytical run. All samples were analyzed in the negative mode by multiple reaction monitoring. The amounts of metabolites of glycolysis, pentose phosphate pathways, tricarboxylic acid cycle as well as nucleotides were determined. To ensure highly accurate quantification, the isotope dilution mass spectrometry (IDMS) method was used. For quantification the addition of full ^{13}C *E. coli* extract which contains a majority of the target metabolites was used, the internal standard. The quantification for each metabolite was first expressed as ^{13}C/^{12}C ratio or as ^{12}C area if the internal ^{13}C standard was not available. For metabolites for which a chemical standard was available, the absolute quantification was calculated from the corresponding calibration curve. For the second and the third experiment (Table 1 and Supplementary Fig. 6a), we used a LTQ Orbitrap Velos™ / Liquid anion exchange chromatography Dionex™ ICS-5000+ Reagent-Free™ HPIC™ equipment. The analyses were carried out on an IC-MS platform of a liquid anion exchange chromatography Dionex™ ICS-5000+ Reagent-Free™ HPIC™ (Thermo Fisher Scientific™, Sunnyvale, CA, USA) system, coupled to a Thermo Scientific™ LTQ Orbitrap Velos™ mass spectrometer (Thermo Fisher Scientific, San Jose, CA, USA) equipped with a heated electrospray ionization probe. Liquid anion exchange chromatography was performed with the Thermo Scientific Dionex ICS-5000+ Reagent-Free HPIC system (Thermo Fisher

Scientific, Sunnyvale, CA, USA) equipped with an eluent generator system (ICS-5000+EG, Dionex) for automatic base generation (KOH). Analytes were separated within 50 min, using a linear KOH gradient elution applied to an IonPac AS11 column (250 x 2 mm, Dionex) equipped with an AG11 guard column (50 x 2 mm, Dionex) at a flow rate of 0.35 ml/min. The gradient program was following: 0 min: 0.5 mM, 1 min: 0.5 mM, 9.5 min: 4.1 mM, 14.6 min: 4.1 mM, 24 min: 9.65 mM, 31.1 min: 90 mM and 43 min: 90 mM, then 43 to 48 min vat 0.5 mM. The column and autosampler temperatures were thermostated at 25°C and 4°C, respectively. The injected sample volume was 15 μl. Measures were performed in triplicates from separate specimens. Mass detection was carried out in a negative electrospray ionization (ESI) mode at a resolution of 60 000 (at 400 m/z) in full-scan mode, with the following source parameters: the capillary temperature was 350°C, the source heater temperature, 300°C, the sheath gas flow rate, 50 arbitrary units (a.u.), the auxiliary gas flow rate, 5 arbitrary units (a.u.), the S-Lens RF level, 60%, and the source voltage, 2.75 kV. Data acquisition was performed using Thermo Scientific Xcalibur software. Metabolites were determined by extracting the exact mass with a tolerance of 5-10 ppm. For quantification the addition of full ^{13}C *E. coli* extract which contains a majority of the target metabolites was used, and quantified as above. Data were processed using TraceFinder 4.1 software. For the third experiment (Supplementary Fig. 6a), the gradient was modified as follows equilibration with 7 mM KOH during 1.0 min; then KOH ramp from 7 to 15 mM, 1–9.5 min; constant concentration 10.5 min; ramp to 45 mM in 10 min; ramp to 70 mM in 3 min; ramp to 100 mM in 0.1 min; constant concentration 8.9 min; drop to 7 mM in 0.5 min; and equilibration at 7 mM KOH for 7.5 min.

5.2. Ethics approval and consent to participate

The mouse lines were maintained at the animal facility Charles Foix (UMS28) under standard conditions with access *ad libitum* to food and water with a 12-h light/dark cycle. The animals under experimentation were transferred to the animal facility of the Institut de la Vision under the agreement obtained April 26^{th,} 2016 and for 5 years of the *direction départementale de la protection des populations de Paris* (B-75-12-02) and principal investigator (T.L.) certificate (N°A-75-1863; OGM n°5080 CA-II). Mice were housed with access *ad libitum* to food and water with a 12-h light/dark cycle of 20–50 lx. All experiments were performed in accordance with the European Community Council Directives of September 22, 2010 (2010/63/UE). The sex and age of animal subjects are: Figs. 1 and S1: ♂ PN60 ± 2 at the start of the standardized procedure. Fig. 2BCD: ♂ PN86 ± 8. Fig. 2FGH: ♂ PN69 ± 6. Fig. S2ABC: ♂ PN53 ± 7. Fig. 3AC, E and S5: ♂ PN60. Fig. 3D: ♂♀ PN71 ± 4. Fig. 4A ♀ PN73. Fig. 4BI and S4: ♂♀ PN63 ± 1. Figs. 5A and S5C: ♂ PN63. Fig. 5BG ♂ PN69 ± 6. Fig. 6A: ♂ PN300. PN330 ± 30. Fig. 6BK and S7G: ♂ PN 561. Fig. S6; ♂♀ PN63 ± 3. Fig. 7: ♂♀ PN471. Fig. S7AE: ♂♀ PN66. Fig. S7F: ♂ PN330 ± 30.

5.3. Availability of data and materials

- Nucleoredoxin-like 2 LTP https://doi.org/10.17632/2rprjfnvk4.1
- Behavior tests of the *Nxnl2* knock-out mouse https://doi.org/10.17632/y6d6zsgfyv.1
- eBrain: DOI 10.25493/4975-NDG
- Metabolomics: DOI 10.17632/yjmhvpp7rf.1

5.4. Animals

The *Nxnl2*$^{-/-}$ mice on BALB/c background were generated previously [2]. The BALB/c (*Nxnl2*$^{+/+}$) mice were used as their wild-type controls. The *Nxnl2*$^{R/R}$ mice was generated at the *Institut Clinique de la Souris* http://www.ics-mci.fr/en/ using embryonic stem cell clones on a C57BL/6-N background from the VelociGene project # VG14768 MMRRC:059676-UCD. These clones were produced using bacterial artificial chromosome (BAC)-based targeting vectors were constructed to replace the coding sequence of the *Nxnl2* gene with a β-galactosidase reporter gene at positions (51,266,695–51,270,168) of the mouse chromosome 13, corresponding to the ATG and TGA of the RdCVF2L mRNA. The mice, generated on a C57BL/6-N background, were genotyped using multiplex PCR with wild-type: 5′-CCGCTTCTAGGACAGATGTCAG-3'and 5′-GGTAGCATCGCAACTTGGATAAC-3′, R allele: 5′-GTGGTTTGTCCAAACTCATCA-3′ and 5′-GAAGTTATCTCGAGTCGCTACCTTAG-3′ primers. The heterozygous mice (*Nxnl2*$^{R/+}$) were produced by crossing with C57BL/6-N, wild-type mice, which were using as negative controls (*Nxnl2*$^{+/+}$, C57BL/6-N).

5.5. Behavior testing

The tests were performed on groups of 12 ♂ *Nxnl2*$^{-/-}$ and *Nxnl2*$^{+/+}$ aged of 2 months at the department of Phenotyping of the *Institut Clinique de la Souris* (Phenotyping - Institut Clinique de la Souris (ics-mci.fr) using standardized procedures and a well-established pipeline [80]. The tests were performed following an ordered process: 1 - Spontaneous activity and food/water intake, 2 - Open-field test (Anxiety-related and social behavior), 3- SHIRPA (General health and basic sensory functions), 4 - Grip test (Sensori-motor abilities), 5 - Traction reflex test/-String test (Sensori-motor abilities), 6 - Rotarod test (Sensori-motor abilities), 7 - Y-maze spontaneous alternation (Learning and memory), 8 - Tail suspension test (Depression-like behavior), 9 - Acoustic startle reactivity and pre-pulse inhibition, 10 - Contextual and cued fear conditioning (Learning and memory), 11 - Hot plate test (Pain sensitivity), 12 - Pentylenetetrazol susceptibility. The water Morris maze test (Learning and memory) was performed on a distinct cohort of 12 ♂ *Nxnl2*$^{-/-}$ and *Nxnl2*$^{+/+}$ aged of 2 months. The Y-maze spontaneous alternation was also performed on an additional cohort of 12 ♂ *Nxnl2*$^{-/-}$ and *Nxnl2*$^{+/+}$ aged of 2 months and on a cohort of 12 ♂ *Nxnl1*$^{-/-}$ and *Nxnl1*$^{+/+}$ aged of 2 months. On testing days, animals were transferred to the antechambers of the experimental room 30 min before the start of the experiment. All experiments were performed between 8:00 a.m. and 4:00 p.m. A resting period of 2 days to 1 week was used between two consecutive tests. Row data are available at https://data.mendeley.com/datasets/y6d6zsgfyv/1.

5.6. LTP recording

Recordings were performed on hippocampal slices of groups of ♂ *Nxnl2*$^{-/-}$ and *Nxnl2*$^{+/+}$ aged of 2 months at E-Phy-Science https://www.e-phy-science.com/ (Figs. 2 and 5). Recordings were also performed on hippocampal slices of groups of ♂ *Nxnl2*$^{-/-}$ and *Nxnl2*$^{+/+}$ aged of 2 months at *Institut du Fer à Moulin* https://ifm-institute.org/en/home/ according to a protocol previously described (Supl. Fig. 2A) [81]. Mice were deeply anesthetized with isoflurane and decapitated. The brain was quickly removed and immersed in ice-cold pre-oxygenated artificial cerebrospinal fluid (aCSF). 400 μm-thick slices were prepared using a vibratome (VT 1000S; Leica Microsystems, Bannockburn, IL), and placed in a holding chamber in aCSF containing: 124 mM NaCl, 3.5 mM KCl, 1.5 mM $MgSO_4$, 2.5 mM $CaCl_2$, 26.2 mM $NaHCO_3$, 1.2 mM NaH_2PO_4, 11 mM glucose, continuously oxygenated (pH = 7.4, 27 °C). Slices were allowed to recover in these conditions from the slicing at least 1 h before recording. For electrophysiological recordings, a single slice was placed in the recording chamber, submerged and continuously superfused with gassed (95% O_2, 5% CO_2) aCSF (28–31 °C) at a constant rate (2 ml min^{-1}) for the reminder of the experiment. Extracellular field excitatory postsynaptic potentials (fEPSPs) were recorded in the *Cornu Ammonis* (CA)1 stratum radiatum using a glass micropipette filled with aCSF. fEPSPs were evoked by the electric stimulation of Schaffer collaterals/commissural pathway at 0.1 Hz with a bipolar tungsten stimulating electrode placed in the stratum radiatum (100 μs duration). Stable baseline fEPSPs were recorded by stimulating at 30% maximal field amplitude for 20 min prior to beginning experiments [single

stimulation every 20 s (3 Hz)]. Synaptic transmission (input/output) curves were constructed to assess basal synaptic transmission in groups of animals. Long-term potentiation (LTP) was induced by the following stimulation protocol: 3 trains of 100 stimulations at 100 Hz at the same stimulus intensity, with a 20 s interval between trains. Following this conditioning stimulus, a 1 h test period was recorded where responses were again elicited by a single stimulation every 20 s (3 Hz) at the same stimulus intensity. Signals were amplified with an Axopatch 200B amplifier (Molecular Devices, Union City, CA) digitized by a Digidata 1550 interface (Axon Instruments, Molecular Devices, Union City, CA) and sampled at 10 kHz. Recordings were acquired using Clampex (Molecular Devices) and analyzed with Clampfit (Molecular Devices, Union City, CA). Row data are available at https://data.mendeley.com/datasets/2rprjfnvk4/1.

5.7. β-galactosidase staining

For β-galactosidase enzymatic staining, two months aged mice were perfused by transcardial perfusion with 4% paraformaldehyde. Brains were removed and fixed by immersion in 4% paraformaldehyde for 2 h followed by incubation in sucrose 30% over-night (ON). Coronal sections were cut at 25 μm on a HM 450 sliding microtome (Thermo Scientific, Waltham, MA USA). For detection of β-galactosidase, sections were rinsed in phosphate-buffered saline (PBS) 1× and incubated for 24 h in staining solution (0.1 M ferricyanide, 0.1 M ferrocyanide, 1 M $MgCl_2$, 20 mg/ml 5-bromo-4-chloro-3-indolyl-β-D-galactopyranoside in PBS 1 × 0.1% Tween®) at 37 °C in a humidified incubator. After washing in PBS, sections were mounted in Fluoromount™ Aqueous Mounting Medium. Slides were scanned at cellular resolution with a Nanozoomer (Hamamatsu, Hamamatsu City, Japan). The profile in the whole *Nxnl2*$^{R/+}$ brain is available at DOI 10.25493/4975-NDG.

5.8. Metabolomic analysis

Metabolomic analysis of standardized hippocampal specimens of ♂ *Nxnl2*$^{-/-}$ and *Nxnl2*$^{+/+}$ aged of 2 months (Fig. 4) or treated ♂ and ♀ *Nxnl2*$^{-/-}$ and *Nxnl2*$^{+/+}$ aged of 2 months (Fig. 5) were performed by the national infrastructure MetaToul https://www6.toulouse.inrae.fr/metatoul/. The brain is extracted from the cranium, making sure not to damage it, then rinsed in PBS. We removed the cerebellum, making sure not to damage the extremities of the 2 lobes and glued the brain on the support of the vibratome, posterior side up. Using a vibratome, we cut 0.5 mm slices lengthwise until reaching the hippocampus. We collected 0.5 mm slices with hippocampal tissue in PBS. Using a binocular magnifying glass, we selected slices with well visible hippocampus morphology (serrated gyrus of the hippocampus visible). We then made three standardized sections using a punch of 2 mm diameter, collected in an Eppendorf tube, and immediately frozen in liquid nitrogen while awaiting sample processing, then further stored at −80 °C. On the day of extraction of the metabolites, we set-up the freeze-mill to cool. The tubes were taken out of −80 °C and left them in liquid nitrogen while waiting. We added 3 steel balls to the tubes containing the hippocampus specimens and immediately placed them in the previously cooled ball mill. We performed 5 × 1 min 30 frequency/sec on a liquid nitrogen-refrigerated CryoMill (Retsch, Haan, Germany). When tissues were powdered, we added 1 ml per tube of methanol/H_2O (80/20) previously cooled to −80 °C plus 120 μl of ^{13}C internal standard. We proceed for 1 min successively with 10 s of vortex +10 s of sonicator +10 s on ice. The specimens were centrifuged for 5 min at 4 °C 13,000 g. The supernatants were collected in a 2-ml Eppendorf tube to which we added 1 ml of cold methanol/H_2O (80/20) mixed to the pellet and performed the same 1 min vortex/sonicator/ice cycle, as before. We centrifuged the tubes for 5 min at 4 °C at 13,000 g, recovered the 2nd supernatant and pooled it with the 1st one. The resulting standardized hippocampal specimens were frozen by immersing in liquid nitrogen and stored at −80 °C pending metabolomic analysis. The specimens were sent on dry-ice. Processed data are available at DOI 10.17632/yjmhvpp7rf.1. Row data are available upon request.

5.9. Recombinant adeno-associated viral (AAV) vector production and validation

Plasmids AAV2/9-2 YF- cytomegalovirus enhancer/chicken β-actin (CMV/CBA)-RdCVF2^{2A}green fluorescent protein (GFP) and AAV2/9-2 YF-CMV/CBA-RdCVF2L^{2A}GFP contain the GFP protein, a self-cleaving 2A peptide upstream of the cDNA of mouse RdCVF2 (Q9D531-4) and mouse RdCVF2L (Q9D531-3) respectively under the control of the CMV/CBA promoter. AAV2/9-2 YF-CMV/CBA-GFP is the negative control. Recombinant AAV was purified via iodixanol gradient ultracentrifugation as described previously [7]. The 40% iodixanol fraction was then buffer-exchanged against PBS supplemented with 0.001% tween-20 and concentrated using ultrafiltration on with a cutoff of 100 kDa (Amicon Ultra-15) to a final volume of 200 μl. DNase-resistant viral genomes in the concentrated stock were then tittered by qPCR relative to standards. Vector concentrations were calculated in viral genomes (vg)/ml with AAV2/9-2 YF-CMV/CBA-GFP at 1.35 × 10^{14} viral genome (vg)/ml, AAV2/9-2 YF-CMV/CBA-RdCVF2^{2A}GFP at 1.16 × 10^{14} vg/ml, and AAV2/9-2 YF-CMV/CBA-RdCVF2L^{2A}GFP at 8.85 × 10^{13} vg/ml. The quality controls were performed by silver staining using ProteoSilve™ Silver Stain Kit (PROT-SIL1, Sigma, St Louis, MI, USA) and the procedure recommended by the supplier. Each lane was loaded with 1 × 10^{10} vg with 100 mM dithiothreitol (DTT) onto a 4–12% gel (Supl. Fig. 5A). Uranyl acetate straining was done according to Ref. [82]. Just before pipetting, microtubes were shaken to resuspend the virus particles. 5 μl of each sample was deposited on a 300-mesh nickel grids with 10 nm formvar and 1 nm carbon film (Electron Microscopy Sciences, USA) side up for 1 min at room temperature to let the virus particles adsorb on the film. Samples were quickly rinsed with one first drop (filtered with a 0.22 μm isopore) of 2.5% w/v uranyl acetate (Prolabo, Fontenay-sous-Bois, France) diluted with ultrapure water, then contrasted 1 min with a second drop of the same solution in the dark. Excess solution was removed using a Whatman grade n°40 ashless filter paper and grids were let dry at room temperature. Observations were performed using a LaB_6 JEM 2100 HC TEM (Jeol, Japan), at 200 kV, spot size 1, condenser aperture 1 (150 μm diameter) and objective aperture 3 (15 μm diameter). Acquisitions were made with a side mounted Veleta charge-coupled device (CCD) camera driven by iTEM software version 5.2 (Olympus, Tokyo, Japan). Images were recorded with a 2k x 2k pixels definition (binning 1 × 1) and a 750 ms exposure time. Quantification of the ratio of empty versus full particles was obtained from the mean of counting of 4 independent images taken at magnification 300, 000 (Supl. Fig. 5B). The intracardiac injection in PN4 mice was done as described previously [7]. PN4 *Nxnl2*$^{-/-}$ or *Nxnl2*$^{+/+}$ mice (BALB/c) aged were injected directly in the heart with 20 μl of viral solution (4 × 10^{12} vg) for AAV2/9-2 YF-CMV/CBA-GFP, AAV2/9-2 YF-CMV/CBA-RdCVF2^{2A}GFP and AAV2/9-2 YF-CMV/CBA-RdCVF2L^{2A}GFP (Fig. 5). ½ AAV2/9-2 YF-CMV/CBA-RdCVF2^{2A}GFP + ½ AAV2/9-2 YF-CMV/CBA-RdCVF2L^{2A}GFP corresponds to 2 × 10^{12} vg of each recombinant vector (Fig. 5). Alternatively, we injected only 10 μl of ½ AAV2/9-2 YF-CMV/CBA-RdCVF2^{2A}GFP + ½ AAV2/9-2 YF-CMV/CBA-RdCVF2L^{2A}GFP which correspond to corresponds to 0.5 × 10^{12} vg of each recombinant vector (Fig. 7).

5.10. Immunohistochemistry and histological staining

Two months aged *Nxnl2*$^{R/+}$ (Fig. 2C) and *Nxnl2*$^{+/+}$ (Fig. 2E) ♂ mice were perfused by transcardial perfusion with 4% paraformaldehyde. Brains were removed and fixed by immersion in 4% paraformaldehyde for 2 h followed by incubation in sucrose 30% ON. Coronal sections were cut at 25 μm on a HM 450 sliding microtome (Thermo Scientific™). After β-galactosidase staining, *Nxnl2*$^{R/+}$ slices were permeabilized in 0.3% Triton X-100 in PBS for 4 min and block in 5% bovine serum

albumin (BSA), 10% normal goat serum (NGS) in PBS for 1h 30 at room temperature (RT). After two washes of 5 min in PBS, slides were incubated ON at 4°C rat monoclonal anti-PLVAP (BD Biosciences, Franklin Lakes, NJ USA Cat# 553849, research resource identifiers (RRID): AB_395086, 1/20) (Fig. 2C), plus rabbit polyclonal anti-GLUT1 antibodies (Alpha-diagnostic, San Antonio, TX, USA, GT11-A, RRID: AB_1616630, 1/100) (Fig. 2D) in 5% bovine serum albumin (BSA), 10% normal goat serum (NGS) in PBS. Slides were washed twice for 10 min in 5% BSA in PBS and once 10 min in 1% BSA, 0.1% tween-20 in PBS at RT, then 1h 30 at room temperature (RT) with anti-rat HRP (Jackson ImmunoResearch, West Grove, PA, USA, RRID: AB_2340639, 1/200) in 2% NGS 0.1% Triton in PBS (Fig. 2C) or in the secondary incubation with anti-rat fluo-λ488 (1/400) and anti-mouse fluo-λ594 (1/400) in 1% BSA, 10% NGS, 0.1% tween-20 (Fig. 2C). *Nxnl2*$^{+/+}$ brain was dissected after intra-cardiac perfusion of in 4% paraformaldehyde/PBS (PFA 4%/PBS) with a peristaltic pump followed by the incubation of (PFA 4%/PBS) ON at 4°C. Tissues were incubated successively in 10, 20 and 30% sucrose at 4°C and embedded in optimal cutting temperature (OCT medium) and then freezing in isopentane cooled in liquid nitrogen between −40 and 45°C. The staining protocol with hematoxylin-eosin is standard with 12 min for hematoxylin and 2 min for eosin on 12 µm horizontal cryostat sections (Fig. 4A). The brain specimens of *Nxnl2*$^{+/+}$ and *Nxnl2*$^{-/-}$, were obtained after intra-cardiac perfusions as above and incubated successively in 10, 20 and 30% sucrose at 4°C and cutting with a slide microtome (HM450, Microm) and a freezer unit with 60 µm sagittal slide. The floating sections with observation of GFP were selected for immunohistochemistry with a chicken polyclonal antibodies anti-GFP (Abcam, Cambridge, MA, USA, Cat# ab13970, RRID: AB_300798, 1/1250) ON at 4°C, then, after 2 h with saturation step with triton 0.1%/PBS and revealed with a secondary goat anti-chicken λ488 (1/600) and with Hoechst 33342 (Invitrogen, Carlsbad, CA, USA) during 1 h at room temperature and imaged with an epifluorescence microscope (Leica, Wetzlar Germany) (Fig. 5A and B and Supl. Fig. 5). Slices were permeabilized in 0.3% Triton X-100 in PBS for 4 min and block in 5% bovine BSA, 10% NGS in PBS for 1h 30 at room temperature (RT). After two washes of 5 min in PBS, slides were incubated ON at 4°C with mouse monoclonal antibody anti-RBFOX3/NeuN (Millipore, Burlington, MA, USA, Cat# MAB377, RRID: AB_2298772, 1/500 dilution) and rabbit polyclonal anti-GFAP antibodies (Agilent, Santa Clara, CA, USA, Cat# N1506, RRID: AB_10013482, 1/500). Slices were washed twice in PBS then incubated 1h 30 at RT with and fluo-λ488 conjugated goat anti-mouse and fluo-λ594 conjugated goat anti-rabbit antibodies (Fig. 6A).

5.11. Western blotting

For western blotting analysis of hippocampal specimens, *Nxnl2*$^{-/-}$ and *Nxnl2*$^{-/-}$ standardized hippocampal specimens (Fig. 4G and H, Supl. Fig. 4G and H) or standardized hippocampal specimens from AAV-treated *Nxnl2*$^{-/-}$ mice (Supl. Fig. 5I and J) were prepared from three 0.5 mm thick vibratome slice of 2 mm Ø, all from 2-month mice. Tissues were sonicated twice 10 s on ice in 50 mM Tris-HCl (pH 7.5), 1 mM EDTA, 1 mM DTT, 1% Triton X-100, 1 mM phenylmethylsulfonyl fluoride (PMSF), 0.14 mM Tosyl-L-lysine chloromethyl ketone hydrochloride (TLCK) in the presence of a cocktail of proteinase inhibitors (P2714, Sigma, St Louis, MI, USA). After 30 min on ice, the extracts were centrifuged 5 min at 12,000 rpm at 4°C and 40 µg of whole cell extracted were loaded on a sodium dodecyl sulfate (SDS) gel and transferred to a 0.22 µm nitrocellulose membrane. The samples were not heated for GLUT1 analysis [7,83]. After Saturation, the membranes were incubated with rabbit polyclonal anti-GLUT1 antibodies (Alpha-diagnostic, San Antonio, TX, USA, GT11-A, RRID: AB_1616630, 1/500), rabbit monoclonal anti-GLUT3 antibody (Abcam, Cambridge, MA, USA, Cat# ab191071, RRID: AB_2736916, 1/1000), mouse monoclonal anti-GLUT4 antibody (Santa Cruz Biotechnology, Santa Cruz, CA, USA, Cat# sc-53566, RRID: AB_629533, 1/100) or chicken polyclonal antibodies anti-GFP (Abcam, Cambridge, MA, USA, Cat# ab13970, RRID: AB_300798, 1/5000) ON at 4°C. The western blots were revealed with anti-rabbit or anti-mouse IgG coupled to peroxidase. The signals do not appear with the secondary antibody alone. After stripping the membrane 15 min at RT using reblot plus strong antibody stripping solution (Millipore, Burlington, MA, USA, 60512), the membranes they were incubated with mouse monoclonal anti-ACTB (Millipore, Burlington, MA, USA, Cat# MAB1501, RRID: AB_2223041, 1/10,000) ON at 4°C and revealed with anti-mouse IgG coupled to peroxidase (Jackson Immunoresearch, West Grove, PA, USA, 1/10,000). Filter binding assay was performed as previously described [4] (Fig. 6B, Supl. Fig. 7C). The human brain specimens were provided by NeuroCEB. After dissection of the brain of 18-month *Nxnl2*$^{+/+}$ an *Nxnl2*$^{-/-}$, the cerebellum was removed. Brain extracts were made in lysis buffer (10 mM Tris HCl, pH 8.0, 150 mM NaCl, 1 mM EDTA, 1% NP40, 1% sodium deoxycholate), sonicated and suspended in PBS 2% SDS. 50 µg of protein extract was filtered through 0.22 µm nitrocellulose membrane using Bio-Dot SF assembly (Bio-Rad, Hertfordshire, UK). The 0.22 µm membrane was probed with mouse monoclonal anti-TAU antibody (Santa Cruz Biotechnology, Santa Cruz, CA, USA, Cat# sc-58860, RRID: AB_785931, 1/500). To study TAU expression, oligomerization and phosphorylation, extracts from 18-month *Nxnl2*$^{+/+}$, *Nxnl2*$^{-/-}$ (untreated and treated), *Mapt*$^{+/+}$ and *Mapt*$^{-/-}$ brains without cerebellum were sonicated twice 10 s on ice in 50 mM Tris-HCl (pH 7.5), 1 mM EDTA, 1 mM DTT, 1% Triton X-100, 1 mM PMSF, 0.14 mM TLCK, a cocktail of proteinase inhibitors (P2714, Sigma) and phosphatase inhibitor cocktail (524627, Calbiochem). After 30 min on ice, the extracts were centrifuged 5 min at 12,000 g at 4°C and 40 µg of the supernatant, the whole cell extracted were loaded with Laemmli buffer on a SDS-gel, then transferred to a 0.45 mm polyvinylidene fluoride (PVDF) membrane (Millipore, Burlington, MA, USA). For oligomerization, a 4–12% Bis-Tris protein gel (ThermoFisher, Cat #NP0322BOX) was used instead of SDS-gel that was run under non-reducing conditions (Fig. 6C). After saturation, the membranes were incubated either with chicken polyclonal antibodies anti-GFP (Abcam, Cambridge, MA, USA, Cat# ab13970, RRID: AB_300798, 1/5000) (Fig. 7A) mouse monoclonal anti-TAU antibody (Santa Cruz Biotechnology, Santa Cruz, CA, USA, Cat# sc-58860, RRID: AB_785931, 1/500) (Fig. 6C and D), mouse monoclonal anti-phosphoTAU^{AT100} antibody (Thermo Fisher Scientific, Sunnyvale, CA, USA Cat# MN1060, RRID: AB_223652, 1/200 (Figs. 6E and 7B) or mouse monoclonal anti-phosphoTAU^{AT8} antibody (Thermo Fisher Scientific, Sunnyvale, CA, USA Cat# MN1020, RRID: AB_223647, 1/200) (Fig. 6F) ON at 4°C. Western blots were revealed with anti-species immunoglobulin (Ig)G coupled to peroxidase (Jackson Immunoresearch, West Grove, PA, USA, 1/15,000). After stripping as above, the membranes were incubated with mouse monoclonal anti-ACTB (Millipore, Burlington, MA, USA, Cat# MAB1501, RRID: AB_2223041, 1/10,000) (Fig. 6H) ON at 4°C and revealed with anti-mouse IgG coupled to peroxidase (Jackson Immunoresearch, West Grove, PA, USA, 1/15,000). After stripping as above, the membranes were incubated with mouse monoclonal anti-ACTB (Millipore, Burlington, MA, USA, Cat# MAB1501, 1/10,000). The quantification was made by respecting the proportion of bands in each piece of membrane assembled as indicated by a chevron (<) (Fig. 6). Extracts from 2-month *Nxnl2*$^{+/+}$ and *Nxnl2*$^{-/-}$ brains without cerebellum were prepared and analyzed with mouse monoclonal anti-phosphoTAU^{AT100} antibody (Thermo Fisher Scientific, Sunnyvale, CA, USA, Cat# MN1060, RRID: AB_223652, 1/200) as above (Supl. Fig. 7aA). After stripping, the membrane was incubated with mouse monoclonal anti-ACTB (Millipore, Burlington, MA, USA, Cat# MAB1501, RRID: AB_2223041, 1/10,000) ON at 4°C and revealed with anti-mouse IgG coupled to peroxidase (Jackson Immunoresearch, West Grove, PA, USA, 1/15,000). After stripping as above, the membranes were incubated with mouse monoclonal anti-ACTB (Millipore, Burlington, MA, USA, Cat# MAB1501, 1/10,000). The membrane was then re-stripped and analyzed for the absence of signal using the secondary antibody alone, then incubated with mouse monoclonal anti-GFAP (Sigma-Aldrich Cat# G3893, RRID: AB_477010, 1/1000) (Supl. Fig. 7B).

5.12. RT-PCR

To analyze the expression of the *Nxnl2* gene and the mRNAs of its two splicing variants, we dissected *area postrema* of 2-month $Nxnl2^{R/R}$ (2♀ and 2♂), $Nxnl2^{R/+}$ (4 ♀) and $Nxnl2^{+/+}$ (2♀ and 2♂) mice and used RNA from $Nxnl2^{+/+}$ and $Nxnl2^{-/-}$ retinas as control [2]. RNA were purified with RNesay minikit (Qiagen, Hilden, Germany) and treated with DNAse I before reverse transcription. PCR was performed with the following primers *RdCVF2*: 5'-AGTGCGGAGGAGATGTTGG-3' and 5′-GCTCTGAAACAATAGCACGGT-3′, *RdCVF2L*: 5'-AGATGTTGGACTT-CATGCGC-3' and 5′- GAAAACATCGGCTGCTTCCA-3′, β*Gal*: 5′-TGACTGTAGGGGCTGATG TTG-3′ and 5′-GGTAAACTGGCTCGGAT-TAGGG-3'. The amplification products were validated by sequencing.

5.12. Statistical analyses

Fig. 1, Supplemental Fig. 1, Fig. 2, Supplemental Fig. 2, Fig. 4, Supplemental Figure 4BD: Student's t-test. Supplemental Fig. 4A: Pearson correlation. Supplemental Fig. 4E: Student's t-test. Fig. 5CF: Two-way ANOVA - repeated measures. Fig. 5G: One-way ANOVA. Supplemental Figure 5BF and J: Student's t-test. Supplemental Fig. 5G: One-way ANOVA. Supplemental Fig. 5H: Two-way ANOVA - repeated measures. Fig. 5J: One-way ANOVA. Supplemental Fig. 6B: Pearson correlation. Supplemental Figure 6CE: One-way ANOVA. Fig. 7 and Supplemental Fig. 7A: Student's t-test. Supplemental Fig. 7C: Pearson correlation.

Funding

This research was funded by the *Agence Nationale pour la Recherche* (ANR, *Maladies neurologiques et maladies psychiatriques*, 2008), *Fondation Plan Alzheimer* (2011), *Fondation Vaincre Alzheimer* (2019). This work was also supported by Inserm, Sorbonne Université, and IHU FOReSIGHT [ANR-18-IAHU-0001].

Authors' contributions

C.J., F.O., E.C., G.M-P., M.C., N.A-A., F.B., Q.C., H.M., L.G. performed the experiments. M.F., D.D., J-C.P., J-C.P. J-A.S. provided scientific and technical expertise. T.L. and C.J. designed the project. T.L. wrote the manuscript. All authors read and approved the final manuscript.

Declaration of competing interest

C.J., J-A.S. and T.L. hold two patents on the use of the *NXNL2* gene products as therapeutic agents (WO2010029130A1 and WO2008148860A1). Correspondence and requests for materials should be addressed to T Léveillard (thierry.leveillard@inserm.fr).

Acknowledgements

We thank Jesús Avila, Floriant Bellvert, Alexis Canette, Orna Corchia, Hana N. Dawson, Charles Duyckaerts Vanessa Ferracane, Stéphane Fouquet, Ram Fridlich, Denis Guedin, Camilla Hagen Blixhavn, John Han, Sandrine Hugues-Ascery, Hamid Meziane, Fabrice Riet, Tania Sorg, Alban Vignaud, Celphedia and Phenomin at the *Institut Clinique de la Souris*, the Electron Microscopy Facility, *Institut de Biologie Paris-Seine* and NeuroCEB for their invaluable help.

Abbreviations

2/3 PG	2/3-phosphoglycerate
a.u.	Arbitrary unit
AAV	Adeno-associated viral
aCSF	Artificial cerebrospinal fluid
BSA	Bovine serum albumin
BSG1	Basigin-1
CA	*Cornu Ammonis*
CCD	Charge-coupled device
CMV/CBA	Cytomegalovirus enhancer/chicken β-actin
CSF	Cerebrospinal fluid
DOI	Digital object identifier
DTT	dithiothreitol
F6P	Fructose-6-phosphate
FBP	fructose 1,6-bisphosphate
fEPSP	Field excitatory postsynaptic potentials
FTDP-17	Frontotemporal dementia with parkinsonism linked to chromosome 17
G6P	glucose-6-phosphate
GFAP	Glial fibrillary acidic protein
GFP	Green fluorescent protein
GSH	Glutathione
HFS	High frequency stimulation
IDMS	Isotope dilution mass spectrometry
Ig	Immunoglobulin
LTP	Long-term potentiation
NFT	Neurofibrillary tangles
NGS	normal goat serum
NMDA	N-methyl-D-aspartate
NXNL1	Nucleoredoxin-like 1 gene
NXNL2	Nucleoredoxin-like 2 gene
ON	Over-night
PBS	Phosphate-buffered saline
PFA	paraformaldehyde
PMSF	Phenylmethylsulfonyl fluoride
PN	Post-natal day
PPP	Pentose phosphate pathway
PTZ	Pentylenetetrazol
PVDF	Polyvinylidene fluoride
RdCVF	Rod-derived cone viability factor
RdCVF2	Rod-derived cone viability factor 2
RdCVF2L	Rod-derived cone viability factor 2, long isoform
RdCVFL	Rod-derived cone viability factor, long isoform
RRID	research resource identifiers
RT	room temperature
SDS	Sodium dodecyl sulfate
SHIRPA	SmithKline Beecham, Harwell, Imperial College, Royal London Hospital, phenotype assessment
TAU	microtubule associated protein τ
TLCK	Tosyl-L-lysine chloromethyl ketone hydrochloride
vg	Viral genome

Appendix A. Supplementary data

Supplementary data to this article can be found online at https://doi.org/10.1016/j.redox.2021.102198.

References

[1] F. Chalmel, T. Leveillard, C. Jaillard, A. Lardenois, N. Berdugo, E. Morel, P. Koehl, G. Lambrou, A. Holmgren, J.A. Sahel, O. Poch, Rod-derived Cone Viability Factor-2 is a novel bifunctional-thioredoxin-like protein with therapeutic potential, BMC Mol. Biol. 8 (2007) 74, https://doi.org/10.1186/1471-2199-8-74.

[2] C. Jaillard, A. Mouret, M.L. Niepon, E. Clerin, Y. Yang, I. Lee-Rivera, N. Ait-Ali, G. Millet-Puel, T. Cronin, T. Sedmak, W. Raffelsberger, B. Kinzel, A. Trembleau, O. Poch, J. Bennett, U. Wolfrum, P.M. Lledo, J.A. Sahel, T. Leveillard, Nxnl2 splicing results in dual functions in neuronal cell survival and maintenance of cell integrity, Hum. Mol. Genet. 21 (10) (2012) 2298–2311, https://doi.org/10.1093/hmg/dds050.

[3] G. Elachouri, I. Lee-Rivera, E. Clerin, M. Argentini, R. Fridlich, F. Blond, V. Ferracane, Y. Yang, W. Raffelsberger, J. Wan, J. Bennett, J.A. Sahel, D.J. Zack, T. Leveillard, Thioredoxin rod-derived cone viability factor protects against photooxidative retinal damage, Free Radic. Biol. Med. 81 (2015) 22–29, https://doi.org/10.1016/j.freeradbiomed.2015.01.003.

[4] T. Cronin, W. Raffelsberger, I. Lee-Rivera, C. Jaillard, M.L. Niepon, B. Kinzel, E. Clerin, A. Petrosian, S. Picaud, O. Poch, J.A. Sahel, T. Leveillard, The disruption of the rod-derived cone viability gene leads to photoreceptor dysfunction and susceptibility to oxidative stress, Cell Death Differ. 17 (7) (2010) 1199–1210, https://doi.org/10.1038/cdd.2010.2.

[5] X. Mei, A. Chaffiol, C. Kole, Y. Yang, G. Millet-Puel, E. Clerin, N. Ait-Ali, J. Bennett, D. Dalkara, J.A. Sahel, J. Duebel, T. Leveillard, The thioredoxin encoded by the rod-derived cone viability factor gene protects cone photoreceptors against oxidative stress, Antioxidants Redox Signal. 24 (16) (2016) 909–923, https://doi.org/10.1089/ars.2015.6509.

[6] E. Clerin, M. Marussig, J.A. Sahel, T. Leveillard, Metabolic and redox signaling of the nucleoredoxin-like-1 gene for the treatment of genetic retinal diseases, Int. J. Mol. Sci. 21 (5) (2020), https://doi.org/10.3390/ijms21051625.

[7] N. Ait-Ali, R. Fridlich, G. Millet-Puel, E. Clerin, F. Delalande, C. Jaillard, F. Blond, L. Perrocheau, S. Reichman, L.C. Byrne, A. Olivier-Bandini, J. Bellalou, E. Moyse, F. Bouillaud, X. Nicol, D. Dalkara, A. van Dorsselaer, J.A. Sahel, T. Leveillard, Rod-derived cone viability factor promotes cone survival by stimulating aerobic glycolysis, Cell 161 (4) (2015) 817–832, https://doi.org/10.1016/j.cell.2015.03.023.

[8] T. Leveillard, Cancer metabolism of cone photoreceptors, Oncotarget 6 (32) (2015) 32285–32286, https://doi.org/10.18632/oncotarget.5963.

[9] Y. Chinchore, T. Begaj, D. Wu, E. Drokhlyansky, C.L. Cepko, Glycolytic reliance promotes anabolism in photoreceptors, eLife 6 (2017), https://doi.org/10.7554/eLife.25946.

[10] R. Fridlich, F. Delalande, C. Jaillard, J. Lu, L. Poidevin, T. Cronin, L. Perrocheau, G. Millet-Puel, M.L. Niepon, O. Poch, A. Holmgren, A. Van Dorsselaer, J.A. Sahel, T. Leveillard, The thioredoxin-like protein rod-derived cone viability factor (RdCVFL) interacts with TAU and inhibits its phosphorylation in the retina, Mol. Cell. Proteomics 8 (6) (2009) 1206–1218, https://doi.org/10.1074/mcp.M800406-MCP200.

[11] C.G. Miller, A. Holmgren, E.S.J. Arner, E.E. Schmidt, NADPH-dependent and -independent disulfide reductase systems, Free Radic. Biol. Med. 127 (2018) 248–261, https://doi.org/10.1016/j.freeradbiomed.2018.03.051.

[12] T. Leveillard, N. Ait-Ali, Cell signaling with extracellular thioredoxin and thioredoxin-like proteins: insight into their mechanisms of action, Oxid. Med. Cell. Longev. 2017 (2017) 8475125, https://doi.org/10.1155/2017/8475125.

[13] T. Leveillard, J.A. Sahel, Metabolic and redox signaling in the retina, Cell. Mol. Life Sci. 74 (20) (2017) 3649–3665, https://doi.org/10.1007/s00018-016-2318-7.

[14] D.S. Knopman, R.C. Petersen, Mild cognitive impairment and mild dementia: a clinical perspective, Mayo Clin. Proc. 89 (10) (2014) 1452–1459, https://doi.org/10.1016/j.mayocp.2014.06.019.

[15] J.A. Clayton, F.S. Collins, Policy: NIH to balance sex in cell and animal studies, Nature 509 (7500) (2014) 282–283, https://doi.org/10.1038/509282a.

[16] T. Wolloscheck, S. Kunst, D.K. Kelleher, R. Spessert, Transcriptional regulation of nucleoredoxin-like genes takes place on a daily basis in the retina and pineal gland of rats, Vis. Neurosci. 32 (2015) E002, https://doi.org/10.1017/S0952523814000352.

[17] P. Satishchandra, T. Mathew, Handbook of Clinical Neurology, Vol 87 (3rd Series) Malformations of the Nervous System, BMJ Publishing Group Ltd, 2008.

[18] K.L. Ellacott, G.J. Morton, S.C. Woods, P. Tso, M.W. Schwartz, Assessment of feeding behavior in laboratory mice, Cell Metabol. 12 (1) (2010) 10–17, https://doi.org/10.1016/j.cmet.2010.06.001.

[19] M. La-Vu, B.C. Tobias, P.J. Schuette, A. Adhikari, To approach or avoid: an introductory overview of the study of anxiety using rodent assays, Front. Behav. Neurosci. 14 (2020) 145, https://doi.org/10.3389/fnbeh.2020.00145.

[20] C.J. Gordon, The mouse thermoregulatory system: its impact on translating biomedical data to humans, Physiol. Behav. 179 (2017) 55–66, https://doi.org/10.1016/j.physbeh.2017.05.026.

[21] M. Adlanmerini, B.J. Carpenter, J.R. Remsberg, Y. Aubert, L.C. Peed, H.J. Richter, M.A. Lazar, Circadian lipid synthesis in brown fat maintains murine body temperature during chronic cold, Proc. Natl. Acad. Sci. U. S. A 116 (37) (2019) 18691–18699, https://doi.org/10.1073/pnas.1909883116.

[22] A.W. Fischer, B. Cannon, J. Nedergaard, Optimal housing temperatures for mice to mimic the thermal environment of humans: an experimental study, Mol. Metabol. 7 (2018) 161–170, https://doi.org/10.1016/j.molmet.2017.10.009.

[23] R.C. Gaspar, J.R. Pauli, G.I. Shulman, V.R. Munoz, An update on brown adipose tissue biology: a discussion of recent findings, Am. J. Physiol. Endocrinol. Metab. 320 (3) (2021) E488–E495, https://doi.org/10.1152/ajpendo.00310.2020.

[24] K. Rodrigues, R.M. Pereira, T.D.P. de Campos, R.F. de Moura, A.S.R. da Silva, D. E. Cintra, E.R. Ropelle, J.R. Pauli, M.B. de Araujo, L.P. de Moura, The role of physical exercise to improve the browning of white adipose tissue via POMC neurons, Front. Cell. Neurosci. 12 (2018) 88, https://doi.org/10.3389/fncel.2018.00088.

[25] N. Kataoka, H. Hioki, T. Kaneko, K. Nakamura, Psychological stress activates a dorsomedial hypothalamus-medullary raphe circuit driving brown adipose tissue thermogenesis and hyperthermia, Cell Metabol. 20 (2) (2014) 346–358, https://doi.org/10.1016/j.cmet.2014.05.018.

[26] N. Sakayori, S. Kato, M. Sugawara, S. Setogawa, H. Fukushima, R. Ishikawa, S. Kida, K. Kobayashi, Motor skills mediated through cerebellothalamic tracts projecting to the central lateral nucleus, Mol. Brain 12 (1) (2019) 13, https://doi.org/10.1186/s13041-019-0431-x.

[27] S.J. Webster, A.D. Bachstetter, P.T. Nelson, F.A. Schmitt, L.J. Van Eldik, Using mice to model Alzheimer's dementia: an overview of the clinical disease and the preclinical behavioral changes in 10 mouse models, Front. Genet. 5 (2014) 88, https://doi.org/10.3389/fgene.2014.00088.

[28] Y. Stukalin, A. Lan, H. Einat, Revisiting the validity of the mouse tail suspension test: systematic review and meta-analysis of the effects of prototypic antidepressants, Neurosci. Biobehav. Rev. 112 (2020) 39–47, https://doi.org/10.1016/j.neubiorev.2020.01.034.

[29] V. Castagne, R.D. Porsolt, P. Moser, Use of latency to immobility improves detection of antidepressant-like activity in the behavioral despair test in the mouse, Eur. J. Pharmacol. 616 (1–3) (2009) 128–133, https://doi.org/10.1016/j.ejphar.2009.06.018.

[30] R. Gomez-Nieto, S. Hormigo, D.E. Lopez, Prepulse inhibition of the auditory startle reflex assessment as a hallmark of brainstem sensorimotor gating mechanisms, Brain Sci. 10 (9) (2020), https://doi.org/10.3390/brainsci10090639.

[31] J. Hur, J.F. Smith, K.A. DeYoung, A.S. Anderson, J. Kuang, H.C. Kim, R.M. Tillman, M. Kuhn, A.S. Fox, A.J. Shackman, Anxiety and the neurobiology of temporally uncertain threat anticipation, J. Neurosci. 40 (41) (2020) 7949–7964, https://doi.org/10.1523/JNEUROSCI.0704-20.2020.

[32] M. Aincy, H. Meziane, Y. Herault, Y. Humeau, Synaptic dysfunction in amygdala in intellectual disorder models, Progr. Neuro-psychopharmacol. Biol. Psychiatr. 84 (Pt B) (2018) 392–397, https://doi.org/10.1016/j.pnpbp.2017.07.028.

[33] J.N. Crawley, What's wrong with my mouse?. Behavioral Phenotyping of Transgenic and Knockout Mice John Wiley & Sons, 2007.

[34] S.G. Wilson, J.S. Mogil, Measuring pain in the (knockout) mouse: big challenges in a small mammal, Behav. Brain Res. 125 (1–2) (2001) 65–73, https://doi.org/10.1016/s0166-4328(01)00281-9.

[35] S. Zhang, X. Jin, Z. You, S. Wang, G. Lim, J. Yang, M. McCabe, N. Li, J. Marota, L. Chen, J. Mao, Persistent nociception induces anxiety-like behavior in rodents: role of endogenous neuropeptide S, Pain 155 (8) (2014) 1504–1515, https://doi.org/10.1016/j.pain.2014.04.026.

[36] X.Y. Lian, F.A. Khan, J.L. Stringer, Fructose-1,6-bisphosphate has anticonvulsant activity in models of acute seizures in adult rats, J. Neurosci. 27 (44) (2007) 12007–12011, https://doi.org/10.1523/JNEUROSCI.3163-07.2007.

[37] A.E. Greene, M.T. Todorova, T.N. Seyfried, Perspectives on the metabolic management of epilepsy through dietary reduction of glucose and elevation of ketone bodies, J. Neurochem. 86 (3) (2003) 529–537, https://doi.org/10.1046/j.1471-4159.2003.01862.x.

[38] P. Andersen, R. Morris, D. Amaral, T. Bliss, J. O'Keefe, The hippocampus Book, Oxford university press, 2006.

[39] Y. Medlej, H. Salah, L. Wadi, S. Saad, R. Asdikian, N. Karnib, D. Ghazal, B. Bashir, J. Allam, M. Obeid, Overview on emotional behavioral testing in rodent models of pediatric epilepsy, Methods Mol. Biol. 2011 (2019) 345–367, https://doi.org/10.1007/978-1-4939-9554-7_20.

[40] E. Pastalkova, P. Serrano, D. Pinkhasova, E. Wallace, A.A. Fenton, T.C. Sacktor, Storage of spatial information by the maintenance mechanism of LTP, Science 313 (5790) (2006) 1141–1144, https://doi.org/10.1126/science.1128657.

[41] G.A. Kerchner, R.A. Nicoll, Silent synapses and the emergence of a postsynaptic mechanism for LTP, Nat. Rev. Neurosci. 9 (11) (2008) 813–825, https://doi.org/10.1038/nrn2501.

[42] S. Lambard, S. Reichman, C. Berlinicke, M.L. Niepon, O. Goureau, J.A. Sahel, T. Leveillard, D.J. Zack, Expression of rod-derived cone viability factor: dual role of CRX in regulating promoter activity and cell-type specificity, PLoS One 5 (10) (2010), e13075, https://doi.org/10.1371/journal.pone.0013075.

[43] T. Léveillard, F. Ouechtati, M. Corsi, F. Blond, Expression profile of the nucleoredoxin-like 2 gene in the mouse brain using a beta-galactosidase knock-in reporter strain, in: EBRAINS, EBRAINS, 2021, https://doi.org/10.25493/4975-NDG.

[44] C.J. Price, T.D. Hoyda, A.V. Ferguson, The area postrema: a brain monitor and integrator of systemic autonomic state, Neuroscientist 14 (2) (2008) 182–194, https://doi.org/10.1177/1073858407311100.

[45] Q.P. Wang, J.L. Guan, W. Pan, A.J. Kastin, S. Shioda, A diffusion barrier between the area postrema and nucleus tractus solitarius, Neurochem. Res. 33 (10) (2008) 2035–2043, https://doi.org/10.1007/s11064-008-9676-y.

[46] M.J. McKinley, D.A. Denton, P.J. Ryan, S.T. Yao, A. Stefanidis, B.J. Oldfield, From sensory circumventricular organs to cerebral cortex: neural pathways controlling thirst and hunger, J. Neuroendocrinol. 31 (3) (2019), e12689, https://doi.org/10.1111/jne.12689.

[47] E.P.S. da Conceicao, S.F. Morrison, G. Cano, P. Chiavetta, D. Tupone, Median preoptic area neurons are required for the cooling and febrile activations of brown adipose tissue thermogenesis in rat, Sci. Rep. 10 (1) (2020) 18072, https://doi.org/10.1038/s41598-020-74272-w.

[48] D. Yu, B. Corbett, Y. Yan, G.X. Zhang, P. Reinhart, S.J. Cho, J. Chin, Early cerebrovascular inflammation in a transgenic mouse model of Alzheimer's disease, Neurobiol. Aging 33 (12) (2012) 2942–2947, https://doi.org/10.1016/j.neurobiolaging.2012.02.023.

[49] N. Maolood, B. Meister, Protein components of the blood-brain barrier (BBB) in the brainstem area postrema-nucleus tractus solitarius region, J. Chem. Neuroanat. 37 (3) (2009) 182–195, https://doi.org/10.1016/j.jchemneu.2008.12.007.

[50] J. Duran, I. Saez, A. Gruart, J.J. Guinovart, J.M. Delgado-Garcia, Impairment in long-term memory formation and learning-dependent synaptic plasticity in mice lacking glycogen synthase in the brain, J. Cerebr. Blood Flow Metabol. 33 (4) (2013) 550–556, https://doi.org/10.1038/jcbfm.2012.200.

[51] N.S. Chandel, Navigating Metabolism, 2015.

[52] Y.R. Yang, S. Song, H. Hwang, J.H. Jung, S.J. Kim, S. Yoon, J.H. Hur, J.I. Park, C. Lee, D. Nam, Y.K. Seo, J.H. Kim, H. Rhim, P.G. Suh, Memory and synaptic plasticity are impaired by dysregulated hippocampal O-GlcNAcylation, Sci. Rep. 7 (2017) 44921, https://doi.org/10.1038/srep44921.

[53] Q. Hu, R.J. Noll, H. Li, A. Makarov, M. Hardman, R. Graham Cooks, The Orbitrap: a new mass spectrometer, J. Mass Spectrom. 40 (4) (2005) 430–443, https://doi.org/10.1002/jms.856.
[54] D.C. Love, J.A. Hanover, The hexosamine signaling pathway: deciphering the "O-GlcNAc code, Sci. STKE 2005 (312) (2005) re13, https://doi.org/10.1126/stke.3122005re13.
[55] D.A. Bradbury, T.D. Simmons, K.J. Slater, S.P. Crouch, Measurement of the ADP: ATP ratio in human leukaemic cell lines can be used as an indicator of cell viability, necrosis and apoptosis, J. Immunol. Methods 240 (1–2) (2000) 79–92, https://doi.org/10.1016/s0022-1759(00)00178-2.
[56] D.A. Buchner, A. Charrier, E. Srinivasan, L. Wang, M.T. Paulsen, M. Ljungman, D. Bridges, A.R. Saltiel, Zinc finger protein 407 (ZFP407) regulates insulin-stimulated glucose uptake and glucose transporter 4 (Glut4) mRNA, J. Biol. Chem. 290 (10) (2015) 6376–6386, https://doi.org/10.1074/jbc.M114.623736.
[57] E.C. McNay, J. Pearson-Leary, GluT4: a central player in hippocampal memory and brain insulin resistance, Exp. Neurol. 323 (2020) 113076, https://doi.org/10.1016/j.expneurol.2019.113076.
[58] D. Dalkara, L.C. Byrne, T. Lee, N.V. Hoffmann, D.V. Schaffer, J.G. Flannery, Enhanced gene delivery to the neonatal retina through systemic administration of tyrosine-mutated AAV9, Gene Ther. 19 (2) (2012) 176–181, https://doi.org/10.1038/gt.2011.163.
[59] D.F. Aschauer, S. Kreuz, S. Rumpel, Analysis of transduction efficiency, tropism and axonal transport of AAV serotypes 1, 2, 5, 6, 8 and 9 in the mouse brain, PLoS One 8 (9) (2013), e76310, https://doi.org/10.1371/journal.pone.0076310.
[60] S.T. Bate, R.A. Clark, The Design and Statistical Analysis of Animal Experiments, Cambridge University Press, 2014.
[61] I.B. Aban, B. George, Statistical considerations for preclinical studies, Exp. Neurol. 270 (2015) 82–87, https://doi.org/10.1016/j.expneurol.2015.02.024.
[62] D. Keller, C. Ero, H. Markram, Cell densities in the mouse brain: a systematic review, Front. Neuroanat. 12 (2018) 83, https://doi.org/10.3389/fnana.2018.00083.
[63] G. Ashrafi, Z. Wu, R.J. Farrell, T.A. Ryan, GLUT4 mobilization supports energetic demands of active synapses, Neuron 93 (3) (2017) 606–615, https://doi.org/10.1016/j.neuron.2016.12.020.
[64] H. Braak, E. Braak, Neuropathological stageing of Alzheimer-related changes, Acta Neuropathol. 82 (4) (1991) 239–259, https://doi.org/10.1007/BF00308809.
[65] U. Rub, K. Del Tredici, C. Schultz, D.R. Thal, E. Braak, H. Braak, The evolution of Alzheimer's disease-related cytoskeletal pathology in the human raphe nuclei, Neuropathol. Appl. Neurobiol. 26 (6) (2000) 553–567, https://doi.org/10.1046/j.0305-1846.2000.00291.x.
[66] R. Afridi, W.H. Lee, K. Suk, Microglia gone awry: linking immunometabolism to neurodegeneration, Front. Cell. Neurosci. 14 (2020) 246, https://doi.org/10.3389/fncel.2020.00246.
[67] H.N. Dawson, A. Ferreira, M.V. Eyster, N. Ghoshal, L.I. Binder, M.P. Vitek, Inhibition of neuronal maturation in primary hippocampal neurons from tau deficient mice, J. Cell Sci. 114 (Pt 6) (2001) 1179–1187.
[68] H. Wesseling, W. Mair, M. Kumar, C.N. Schlaffner, S. Tang, P. Beerepoot, B. Fatou, A.J. Guise, L. Cheng, S. Takeda, J. Muntel, M.S. Rotunno, S. Dujardin, P. Davies, K. S. Kosik, B.L. Miller, S. Berretta, J.C. Hedreen, L.T. Grinberg, W.W. Seeley, B. T. Hyman, H. Steen, J.A. Steen, Tau PTM profiles identify patient heterogeneity and stages of alzheimer's disease, Cell 183 (6) (2020) 1699–1713, https://doi.org/10.1016/j.cell.2020.10.029, e13.
[69] L.C. Byrne, D. Dalkara, G. Luna, S.K. Fisher, E. Clerin, J.A. Sahel, T. Leveillard, J. G. Flannery, Viral-mediated RdCVF and RdCVFL expression protects cone and rod photoreceptors in retinal degeneration, J. Clin. Invest. 125 (1) (2015) 105–116, https://doi.org/10.1172/JCI65654.
[70] N.E. Fultz, G. Bonmassar, K. Setsompop, R.A. Stickgold, B.R. Rosen, J.R. Polimeni, L.D. Lewis, Coupled electrophysiological, hemodynamic, and cerebrospinal fluid oscillations in human sleep, Science 366 (6465) (2019) 628–631, https://doi.org/10.1126/science.aax5440.
[71] D. Tokar, L. van Ekeris, P.J. Linser, J.D. Ochrietor, Characterization of the expression of basigin gene products within the pineal gland of mice, Cell. Mol. Neurobiol. 37 (6) (2017) 1141–1145, https://doi.org/10.1007/s10571-016-0441-5.
[72] P. Haunhorst, C. Berndt, S. Eitner, J.R. Godoy, C.H. Lillig, Characterization of the human monothiol glutaredoxin 3 (PICOT) as iron-sulfur protein, Biochem. Biophys. Res. Commun. 394 (2) (2010) 372–376, https://doi.org/10.1016/j.bbrc.2010.03.016.
[73] T.T. Huang, D. Leu, Y. Zou, Oxidative stress and redox regulation on hippocampal-dependent cognitive functions, Arch. Biochem. Biophys. 576 (2015) 2–7, https://doi.org/10.1016/j.abb.2015.03.014.
[74] S.A. Lipton, Y.B. Choi, H. Takahashi, D. Zhang, W. Li, A. Godzik, L.A. Bankston, Cysteine regulation of protein function–as exemplified by NMDA-receptor modulation, Trends Neurosci. 25 (9) (2002) 474–480, https://doi.org/10.1016/s0166-2236(02)02245-2.
[75] T.L. Dutka, G.D. Lamb, Na+-K+ pumps in the transverse tubular system of skeletal muscle fibers preferentially use ATP from glycolysis, Am. J. Physiol. Cell Physiol. 293 (3) (2007) C967–C977, https://doi.org/10.1152/ajpcell.00132.2007.
[76] N.J. Gerkau, R. Lerchundi, J.S.E. Nelson, M. Lantermann, J. Meyer, J. Hirrlinger, C. R. Rose, Relation between activity-induced intracellular sodium transients and ATP dynamics in mouse hippocampal neurons, J. Physiol. 597 (23) (2019) 5687–5705, https://doi.org/10.1113/JP278658.
[77] S. Fujii, ATP- and adenosine-mediated signaling in the central nervous system: the role of extracellular ATP in hippocampal long-term potentiation, J. Pharmacol. Sci. 94 (2) (2004) 103–106, https://doi.org/10.1254/jphs.94.103.
[78] S. Carmona, J. Hardy, R. Guerreiro, The genetic landscape of Alzheimer disease, Handb. Clin. Neurol. 148 (2018) 395–408, https://doi.org/10.1016/B978-0-444-64076-5.00026-0.
[79] J.C. Lambert, S. Heath, G. Even, D. Campion, K. Sleegers, M. Hiltunen, O. Combarros, D. Zelenika, M.J. Bullido, B. Tavernier, L. Letenneur, K. Bettens, C. Berr, F. Pasquier, N. Fievet, P. Barberger-Gateau, S. Engelborghs, P. De Deyn, I. Mateo, A. Franck, S. Helisalmi, E. Porcellini, O. Hanon, I. European Alzheimer's Disease Initiative, M.M. de Pancorbo, C. Lendon, C. Dufouil, C. Jaillard, T. Leveillard, V. Alvarez, P. Bosco, M. Mancuso, F. Panza, B. Nacmias, P. Bossu, P. Piccardi, G. Annoni, D. Seripa, D. Galimberti, D. Hannequin, F. Licastro, H. Soininen, K. Ritchie, H. Blanche, J.F. Dartigues, C. Tzourio, I. Gut, C. Van Broeckhoven, A. Alperovitch, M. Lathrop, P. Amouyel, Genome-wide association study identifies variants at CLU and CR1 associated with Alzheimer's disease, Nat. Genet. 41 (10) (2009) 1094–1099, https://doi.org/10.1038/ng.439.
[80] A. Dubos, H. Meziane, G. Iacono, A. Curie, F. Riet, C. Martin, N. Loaec, M. C. Birling, M. Selloum, E. Normand, G. Pavlovic, T. Sorg, H.G. Stunnenberg, J. Chelly, Y. Humeau, G. Friocourt, Y. Herault, A new mouse model of ARX dup24 recapitulates the patients' behavioral and fine motor alterations, Hum. Mol. Genet. 27 (12) (2018) 2138–2153, https://doi.org/10.1093/hmg/ddy122.
[81] N. Le Roux, C. Cabezas, U.L. Bohm, J.C. Poncer, Input-specific learning rules at excitatory synapses onto hippocampal parvalbumin-expressing interneurons, J. Physiol. 591 (7) (2013) 1809–1822, https://doi.org/10.1113/jphysiol.2012.245852.
[82] J.C. Grieger, S.M. Soltys, R.J. Samulski, Production of recombinant adeno-associated virus vectors using suspension HEK293 cells and continuous harvest of vector from the culture media for GMP FIX and FLT1 clinical vector, Mol. Ther. 24 (2) (2016) 287–297, https://doi.org/10.1038/mt.2015.187.
[83] A. Rath, M. Glibowicka, V.G. Nadeau, G. Chen, C.M. Deber, Detergent binding explains anomalous SDS-PAGE migration of membrane proteins, Proc. Natl. Acad. Sci. U. S. A. 106 (6) (2009) 1760–1765, https://doi.org/10.1073/pnas.0813167106.